

HIGH-RESOLUTION NEAR-INFRARED IMAGING OF SUBMILLIMETER GALAXIES

Paula Aguirre^{1,2}, Andrew J. Baker³, Felipe Menanteau³,
Dieter Lutz⁴ and Linda J. Tacconi⁴

ABSTRACT

We present F110W ($\sim J$) and F160W ($\sim H$) observations of ten submillimeter galaxies (SMGs) obtained with the *Hubble Space Telescope*'s (*HST*'s) NICMOS camera. Our targets have optical redshifts in the range $2.20 \leq z \leq 2.81$ confirmed by millimeter CO or mid-IR spectroscopy, guaranteeing that the two bands sample the rest-frame optical with the Balmer break falling between them. Eight of ten are detected in both bands, while two are detected in F160W only. We study their F160W morphologies, applying a maximum-deblending detection algorithm to distinguish multiple- from single-component configurations, leading to reassessments for several objects. Based on our NICMOS imaging and/or previous dynamical evidence we identify five SMGs as multiple sources, which we interpret as merging systems. Additionally, we calculate morphological parameters asymmetry (A) and Gini coefficient (G); thanks to our sample's limited redshift range we recover the trend that multiple-component, merger-like morphologies are reflected in higher asymmetries. We analyze the stellar populations of nine objects with F110W/F160W photometry, using archival *HST* optical data when available. For multiple systems, we are able to model the individual *components* that build up an SMG. With the available data we cannot discriminate among star formation histories, but we constrain stellar masses and mass ratios for merger-like SMG systems, obtaining a mean $\log(M_*/M_\odot) = 10.9 \pm 0.2$ for our full sample, with individual values $\log(M_*/M_\odot) \sim 9.6 - 11.8$. The morphologies

¹Departamento de Astronomía, Pontificia Universidad Católica de Chile, Santiago, Chile; paguirre@astro.puc.cl

²Departamento de Ciencias Físicas, Facultad de Ciencias Exactas, Universidad Andrés Bello, Santiago, Chile

³Department of Physics and Astronomy, Rutgers, The State University of New Jersey, 136 Frelinghuysen Road, Piscataway, NJ 08854-8019, USA; ajbaker@physics.rutgers.edu, felipe@physics.rutgers.edu

⁴Max-Planck-Institut für Extraterrestrische Physik, Postfach 1312, D-85741 Garching, Germany; lutz@mpe.mpg.de, linda@mpe.mpg.de

and mass ratios of the least and most massive systems match the predictions of the major-merger and cold accretion SMG formation scenarios, respectively, suggesting that both channels may have a role in the population’s origin.

Subject headings: galaxies: high-redshift, galaxies: interactions, galaxies: stellar content, galaxies: structure

1. Introduction

Hierarchical scenarios for structure formation posit that the evolving mass function of galaxies is driven by the evolving mass function of dark matter halos (e.g., Mo & White 2002) at all redshifts. In this paradigm, increasingly large numbers of increasingly massive galaxies will form through a mixture of “wet” (gas-rich) and “dry” (gas-poor) mergers, along with the accretion of intergalactic gas. The simplest version of this picture would invoke a direct proportionality between dark and luminous matter, as might be suggested by the observed correlation between clustering of high-redshift UV-selected galaxies and rest-frame UV luminosity, which is roughly proportional to galaxy mass (Ouchi et al. 2004; Adelberger et al. 2005; Hildebrandt et al. 2009). However, results from halo occupation models now indicate that the stellar-to-halo mass (SHM) relationship is more complex; it has a characteristic peak at a halo mass $\sim 10^{12}M_{\odot}$, and declines toward both smaller and larger mass, more steeply in the former case (Somerville et al. 2009; Moster et al. 2010; Behroozi et al. 2012; Yang et al. 2012). These variations in the SHM relationship are explained by the interplay of feedback from supernovae, which is most effective in low-mass halos, and from active galactic nuclei (AGNs), which becomes more efficient in high-mass halos (e.g., Shankar et al. 2006; Somerville et al. 2008). Beyond the form of the SHM relationship, it has also been shown that the peak in star formation efficiency shifts to higher halo masses at higher redshift (e.g., Wang et al. 2012; Wake et al. 2011; Moster et al. 2013), a result that adds to several lines of mounting evidence suggesting that stellar mass build-up happened much earlier in the *most* massive rather than in the least massive galaxies (e.g., Cowie et al. 1996; Marconi et al. 2004; Thomas et al. 2005; Cimatti et al. 2006; Bundy et al. 2006; Kannappan et al. 2009), a trend known as “cosmic downsizing.”

Bright submillimeter galaxies (SMGs; Blain et al. 2002, and references therein) represent a key population in tracing the cosmic history of mass assembly. Their high ($\sim 10^{13} L_{\odot}$) luminosities appear to be powered mainly by star formation, based on the relative faintness of their X-ray counterparts (Alexander et al. 2005) as well as their mid-IR spectra (Lutz et al. 2005; Valiante et al. 2007; Menéndez-Delmestre et al. 2007; Pope et al. 2008), while detections of large molecular gas reservoirs demonstrate that SMGs are *massive* (\geq

$5 - 10 \times 10^{10} M_{\odot}$) as well as luminous (Frayser et al. 1998, 1999; Genzel et al. 2003; Neri et al. 2003; Greve et al. 2005; Tacconi et al. 2006). Bright ($S_{850\mu\text{m}} > 5 \text{ mJy}$) SMGs at $z \sim 2$ have all the properties expected for the progenitors of the most massive local spheroids, caught at a crucial juncture in their assembly (e.g., Smail et al. 2002; Swinbank et al. 2004, 2006; Targett et al. 2011).

Explaining the origin(s) of these high star formation rates and masses has proved to be more difficult. SMGs’ large, complex rest-UV and radio morphologies (Chapman et al. 2003, 2004; Engel et al. 2010) provide some evidence that their intense starbursts have been triggered by mergers. Semi-analytic models explaining SMGs’ observed number counts suggest that short of a top-heavy initial mass function (IMF; Baugh et al. 2005), we *need* multiple early-stage mergers to account for some fraction of the population (Hayward et al. 2011). In contrast, given recent theoretical predictions that accretion of cold gas along filaments can hasten the coalescence of baryons within massive haloes at high redshift (Dekel & Birnboim 2006; Kereš et al. 2005, 2009), Davé et al. (2010) have proposed that cold flows rather than mergers can account for at least some fraction of the SMG population. In this scenario, SMGs would correspond to super-sized, very massive ($\sim 10^{11} - 10^{12} M_{\odot}$) versions of ordinary star-forming galaxies, fed with gas from minor mergers or smooth cold accretion at rates comparable to their star formation rates, which after quenching its star formation by some mechanism(s) evolve into systems like the brightest group ellipticals seen today.

Distinguishing between the merger and cold flow scenarios for SMGs’ striking properties is complicated in two respects by their extreme obscuration at short (i.e., rest-UV) wavelengths. First, high extinction makes SMGs rather difficult targets for redshift determination; successful efforts have required the use of radio maps and blind optical spectroscopy that can be confirmed with CO detections (Chapman et al. 2003, 2005; Neri et al. 2003; Greve et al. 2005), of mid-IR spectroscopy of polycyclic aromatic hydrocarbon (PAH) features (Lutz et al. 2005; Valiante et al. 2007; Menéndez-Delmestre et al. 2007; Pope et al. 2008), or of CO spectroscopy with dedicated, ultrawide-bandwidth instruments (e.g., Swinbank et al. 2010a; Frayer et al. 2011; Lupu et al. 2012; Harris et al. 2012). Such challenges have made it difficult to assemble large and homogeneous SMG samples for statistical analyses. Second, patchy dust screens have made it difficult to interpret the morphologies and masses of SMGs’ stars in the rest-frame UV. Initial efforts have concluded that SMGs have large stellar masses to match their gas masses (Smail et al. 2004; Hainline et al. 2011), but that they are not more likely to appear as major mergers in the rest-frame UV/optical than more typical, lower-luminosity galaxies at the same epoch (Swinbank et al. 2010b).

The physical properties of SMGs’ stellar populations can be better examined in the rest-frame optical, where dust obscuration is less dramatic than in the rest-frame UV. Hence, we

have undertaken a program of high-resolution, rest-frame optical imaging of an SMG sample in a well-defined redshift range using the *Hubble Space Telescope* (*HST*). In this paper, we exploit *HST*’s exceptional resolution to spatially resolve SMGs, characterize their morphologies, identify multiple-component systems that may be interpreted as galaxy mergers, and study the stellar populations in individual merging *components* as well as in single SMGs. We combine our new near-infrared photometry with archival *HST* optical data to derive stellar population synthesis (SPS) models and estimate stellar masses for each component in single and multiple SMG systems, then computing the mass ratios for merger-like systems. In this way, and to the extent that the merger scenario is correct, our goal is to advance our understanding of the progenitors that coalesce to form a massive SMG.

We explain the selection of our sample in Section 2. Section 3 describes the acquisition and reduction of our near-infrared observations, and of complementary optical *HST* data that we have retrieved from the archive in order to do a more complete modeling of our SMGs’ stellar populations. In Section 4 we describe the method we use to distinguish multiple-component SMG systems and measure individual magnitudes for each component, and we report the results of this analysis for each target. We also measure several structural parameters and investigate their correlation with the existence of multiple or single components in SMGs; this analysis is presented in Section 5. In Section 6, we describe our SPS modeling of SMGs and SMG components, and in Section 7 we discuss our measured stellar masses. Our conclusions are summarized in Section 8. Throughout this paper we use a flat $\Omega_\Lambda = 0.7$ cosmology with $H_0 = 70 \text{ km s}^{-1} \text{ Mpc}^{-1}$, and a Chabrier (2003) IMF.

2. Sample

We selected a sample of 10 SMGs for high-resolution near-infrared imaging with *HST* Near Infrared Camera and Multi-Object Spectrometer (NICMOS) in both F110W ($\sim J$) and F160W ($\sim H$) with the aim of studying their rest-frame optical morphologies, modeling their stellar populations, and estimating their stellar masses. The targets were chosen in 2007 January and already at that time had optical redshifts confirmed by the published detection of a millimeter CO line (Frayser et al. 1998, 1999; Neri et al. 2003; Sheth et al. 2004; Greve et al. 2005; Tacconi et al. 2006) and/or a mid-infrared PAH feature (Menéndez-Delmestre et al. 2007; Valiante et al. 2007), both tracers that are closely linked to the far-IR peak of a galaxy’s bolometric emission. We also required that each target’s (robust) redshift lay in the range $1.75 \leq z \leq 3$, placing its 4000 Å break between the centers of the F110W and F160W filters, so that we could exploit our two-band imaging to constrain each target’s stellar population and extinction in a spatially resolved sense. Finally, since we desired reliable

measurements of F110W–F160W ($\sim J-H$) colors for constraining spatially resolved stellar populations, each target had to be observed and detected in both J and K when imaged from the ground (Iverson et al. 1998; Bertoldi et al. 2000; Smail et al. 2002, 2004; Frayer et al. 2003; Borys et al. 2005; Takata et al. 2006), so as to ensure high signal-to-noise ratio (S/N) detections in both J and H bands. The final sample of SMGs and their redshifts are listed in Table 1. Two of our targets (SMM J16368+4057 and SMM J16371+4053) already had F160W data obtained by a previous *HST* program (PID: 9856, PI : Chapman), so we only observed them in band F110W.

3. Observations and data reduction

3.1. Near-infrared Data

Our selected SMGs were observed in the near-infrared F110W ($\sim J$) and F160W ($\sim H$) bands using the NICMOS (NICMOS; Thompson et al. 1998) and Wide Field Camera 3 (WFC3; Kimble et al. 2008) on the *Hubble Space Telescope* (PID = 11143, PI = Baker). As detailed in Table 1, F110W images were obtained using the NIC2 camera, which provides a $19''.2 \times 19''.2$ field of view and a plate scale of $0''.075 \text{ pixel}^{-1}$. In the case of the F160W data, six targets were observed with NIC2 and two with WFC3/IR, which has a $136'' \times 123''$ field of view and $0''.13$, pixels. For the remaining pair, we retrieved existing NIC2 archival data. All new observations took place between 2007 October and 2009 December and used the MULTIACCUM readout mode and a four-point dither pattern to optimize cosmic ray removal.

Our NICMOS F110W and F160W observations were processed using the STSDAS IRAF package (Bushouse & Simon 1994). Each exposure was calibrated using the routine `calnica` and corrected for the “pedestal” and “erratic middle column” effects (Bushouse et al. 1997; Thatte et al. 2009); mosaicking of the dithered datasets was performed using `calnicb` (Bushouse et al. 1997).

In the case of WFC3 data, calibration of raw files was done with the IRAF `calwf3` pipeline (Quijano et al. 2009). The resulting calibrated images showed a multiplicative offset in the signal level of each detector quadrant, which we rectified by multiplying the lower left, upper left, upper right, and lower right portions of each image by factors of 0.992, 1.004, 0.987, and 1.017 respectively (Petro & Baggett 2009). The dithered, calibrated exposures were finally mosaicked using `MultiDrizzle` (Koekemoer et al. 2003), with parameter `pix_frac=1` and an output pixel size of $0''.075 \text{ pixel}^{-1}$ in order to match the NIC2 resolution.

3.2. Optical Data

For better modeling of the stellar populations in our SMG sample, we supplemented our new near-infrared observations with archival *HST* optical imaging of our targets. Some of our targets have also been observed with ground-based telescopes, but to study the stellar populations in components of SMGs we require the high spatial resolution provided by *HST*. We compiled optical observations previously obtained with the Advanced Camera for Surveys (ACS; Ford et al. 1998) for the targets listed in Table 2, which presents the exposure times and details of each retrieved dataset. All ACS imaging used the Wide Field Channel (WFC), with a field of view of $202'' \times 202''$, and plate scale $0''.05 \text{ pixel}^{-1}$. The raw images were calibrated with the STSDAS `calacs` routine and dithered frames were combined using `MultiDrizzle` with the same parameters as for the WFC3 data. For SMM J123707+621410, however, we downloaded the reduced images and weight maps from the Great Observatories Origins Deep Survey (GOODS) *HST*/ACS Treasury Program v2.0 release (Giavalisco et al. 2004); these had a pixel scale of $0''.30 \text{ pixel}^{-1}$, which we drizzled to match the $0''.075 \text{ pixel}^{-1}$ resolution of our NICMOS images.

We aligned all available infrared and optical images for each target to the F160W frame, where the S/N is highest. We measured centroids for the few objects we could identify in each target’s image set, calculated the average x and y displacements relative to the F160W image, and shifted each image accordingly. No image rotations were required. In general, all ACS images were aligned to within ~ 1 pixel ($0''.075$) of each other, but there were shifts relative to the F160W band ranging from $\sim 1''.1$ to $\sim 0''.3$ in R.A. and decl. The F110W images have average R.A. and decl. shifts of $0''.3$ and $0''.15$, respectively.

The described data reduction process produced infrared and optical images that appear flat and free of cosmetic defects and have low background noise. All the final near-infrared and optical images are presented in Figure 1, and discussed in detail in Section 4.2.

3.3. Astrometric Accuracy

To estimate the astrometric accuracy of our infrared images, we checked the positions of all known objects in our targeted fields. For the NICMOS data, we identified five and six sources from the Hubble Deep Field North near-infrared (H , K') catalog of Capak et al. (2004) in the fields of SMM J123549.44+621536.8 and SMM J123707+621410, respectively. This catalog has an astrometric accuracy of $0''.03$, and our mean position error relative to its coordinates is $0''.37$, which gives a total estimated positional error of $0''.40$. For the WFC3 images, we matched two sources from the Sloan Digital Sky Survey (SDSS) Data Release

6 in the field of SMM J16371+4053 and obtained a mean astrometric error of $0''.30$, which combined with a $0''.1$ uncertainty in the SDSS coordinates (Pier et al. 2003) gives a total estimated uncertainty of $0''.40$ for the WFC3 astrometry as well.

3.4. PSF Matching

For accurate color calculations, all images were convolved to match the widest point-spread function (PSF), which defined our lowest resolution and corresponded to the F160W image for those images observed with NICMOS in both infrared bands, and to the F850LP image for targets observed with WFC3. We used the Tiny Tim web-based application to produce model PSFs for each band and for each target’s specific position on the detector, and calculated the transformation kernels between them and the reference PSF with IRAF’s `psfmatch`. We then applied the transformation kernels to the aligned science images and performed a Fourier convolution using `fconvolve`, which multiplies the Fourier transforms of the input array and kernel and then takes the inverse transform to return a real-space image. This method worked successfully for all targets except for the very bright point source in SMM J02399–0136, for which we instead approximated the PSF as a simple two-dimensional Gaussian model with the same full-width at half-maximum (FWHM) as the Tiny Tim model, and convolved to the F160W Gaussian model following the procedure described above.

4. Image Analysis

4.1. Detection and Photometry

Using the known coordinates of our targets, we ran SExtractor (Bertin & Arnouts 1996) in `ASSOC` mode to select the pixels belonging to each source and measure magnitudes and S/Ns. Since the 4000 \AA break falls between our infrared filters, all targets are brighter in F160W than in F110W, so we chose the former as the reference for detection and used SExtractor’s output segmentation images to measure magnitudes in all remaining infrared and optical bands.

To identify substructure or multiple components in our SMGs and study the stellar properties of each component, we need to disentangle their light profiles and define separate photometry apertures for each individual element. To this end, we ran SExtractor with a $\sigma = 2.5$ threshold and *maximum* deblending (`deblend_mincont=0`), so that local peaks in the light profile were distinguished as separate objects and we could pinpoint the position and extension of each component. The final photometry apertures used for each object are

indicated in the stamps presented in Figure 1.

In addition to visual and photometric identification of SMG components, we were also interested in measuring morphological parameters and assessing possible correlations with our single versus multiple-system classifications. In this context, we aim to extract the whole galaxy as a single object, so that possible substructures or clumps are included in the calculated morphological parameters. In addition, for coherent comparison between bands we must select the same area in each frame, so that any variations with wavelength reflect true morphological differences and not selection biases. For these reasons, we ran SExtractor with a lower detection threshold ($\sigma = 2.0$) and minimum deblending (`deblend_mincont=1.0`) on all F160W images, and used the resulting segmentation in the calculations described in Section 5.

For each individual object or component, the integrated flux in each filter was calculated as the sum of all pixel values inside the SExtractor segmentation region, and the local sky mean value (μ_{sky}) and dispersion (σ_{sky}) were estimated over a $0''.5$ wide annulus centered on the target position and located at a radius between $1''.5$ and $2''.5$ so as to avoid nearby sources. The sky-corrected flux was then calculated as $F_{\text{corrected}} = F_{\text{total}} - \mu_{\text{sky}} N_{\text{pix}}$, where N_{pix} is the number of selected pixels. Uncertainties in the measured flux correspond to the sky noise, corrected so as to take into account the difference in areas over which the sky noise and the total flux were measured. The final formula used was $\sigma_{\text{flux}} = \sigma_{\text{sky}} \sqrt{N_{\text{pix}}(1 + N_{\text{pix}}/N_{\text{sky}})}$ where σ_{sky} is the standard deviation among pixels inside the blank annulus used to estimate the local sky value, N_{sky} is the number of pixels in the sky annulus, and N_{pix} is the number of pixels over which the total flux was summed. For WFC3 and ACS images, we also considered the correlated noise introduced by the drizzling process due to the combination of images with partial pixel overlap, and included it in our error estimates following the prescription in Appendix 6 of Casertano et al. (2000).

4.2. Results for Individual Sources

In the following paragraphs we describe our near-infrared observations for each target, and discuss our results in the context of previous work in the literature, taking into account as well the optical data we have retrieved from the *HST* archive. We give special attention to those systems where we have extracted two or more components, which we generally interpret as the building blocks that will merge to form an SMG. Near-infrared and optical magnitudes measured for each object are reported in Table 3, including corrections for lensing magnification when appropriate, and in Figure 1 we present multi-band *HST* imaging for each target.

4.2.1. Multi-component SMGs

SMM J02399–0136 is the brightest source ($S(850\mu\text{m}) = 23.0$ mJy; Smail et al. 2002) detected in the SCUBA Lens Survey (Smail et al. 1997), and was identified by Ivison et al. (1998) as a hyperluminous galaxy at $z = 2.803 \pm 0.003$ lensed by the foreground cluster A370. Detection of CO(3–2) emission by Frayer et al. (1998) revealed a large reservoir of molecular gas, indicating a star-formation origin for the high rest-frame infrared luminosity. Optical imaging and spectroscopy by Ivison et al. (1998) revealed a double counterpart formed by a bright, compact component (L1) hosting a narrow-line AGN (Villar-Martín et al. 1999; Vernet & Cimatti 2001), and a fainter, diffuse companion (L2) associated with Ly α and H α emission indicative of a strong starburst.

Ivison et al. (2010) combined various of the above datasets with new CO(1–0) mapping with the Jansky Very Large Array and high-resolution optical and infrared imaging to study the mass and distribution of the stars, gas, and dust in SMM J02399–0136. Their CO(1–0) map revealed a $\sim 10^{11} M_{\odot}$ reservoir of cold molecular gas extended over 25 kpc in the source plane, encompassing sources L1 and L2, and deep multiwavelength imaging led to the identification of two additional components located to the north of L1 and to the southwest of L2, respectively named L1N and L2SW (see Figure 1 in Ivison et al. 2010). The former was identified as a bright, compact source located ~ 8 kpc north of L1, while the latter corresponded to a red feature that lies southeast of L1 and southwest of L2, emitting strongly in the IRAC bands. The total gravitational magnification derived by Ivison et al. (2010) at the position of SMM J02399–0136 is 2.38 ± 0.08 , which we have used to correct all source-plane quantities that are reported here.

The identification of L1N and especially L2SW by Ivison et al. (2010) relied strongly on the NICMOS imaging obtained through our observing program, which we reuse here in combination with ACS optical imaging to study in greater detail the morphology and stellar population of each component. We have reexamined these data and find that the emission associated with L2SW is visible not only to the southeast of L1, but also to its northwest, reaching out approximately $1''.3$ in this direction. We therefore conclude that L1 is not separate from but actually overlaps with a starburst component that extends along $\sim 3''.8$ in the SE–NW direction, and that appears bright and continuous in the F160W image but is more fragmented and clumpy in F110W and in the optical bands, indicating structured obscuration. As indicated in Figure 1, we refer to this component as L1sb through the rest of this work. We measured its magnitude in the different bands excluding the contribution of the AGN component located in L1, which was modeled as a point source and removed from all of the images. The point source model was generated using GALFIT (Peng et al. 2002) on the F475W image, where the emission is dominated by the AGN; for each of the

(PSF-matched) remaining bands we scaled the model according to the flux measured inside a circular aperture of the same size as the image’s PSF FWHM, and subtracted the result from the original image. This procedure removed most of the compact emission at the position of L1 from the optical F475W and F675W images, leaving only $\sim 4\%$ residuals, which could be due to small deviations from the assumed roundness of the source. However, for the infrared F110W and F160W data, and to a lesser extent for F814W, there is significant residual emission at the position of L1, even after point source subtraction. This emission extends over a radius of $\sim 0''.3$ in all three bands and has a slightly irregular structure that is most noticeable in F814W; we attribute it to a strong starburst immediately surrounding the AGN.

The final apertures used for each component are plotted in Figure 1, which presents the point-source-subtracted images. The apparent magnitudes are presented in Table 3, including the correction for gravitational magnification.

SMM J04431+0210 was first detected by the SCUBA Lens Survey (Smail et al. 1997) in the field of the cluster MS 0440+0204, close to a bright spiral galaxy at $z = 0.18$, and it associated with the extremely red object N4 (Smail et al. 1999). Smail et al. (2002) report a flux density $S(850\mu\text{m}) = 7.2 \pm 1.5$ mJy and a lens magnification of 4.4, which we also adopt. It lies at $z = 2.51$ as measured from optical spectroscopy (Frayser et al. 2003) and detection of the CO(3–2) line (Neri et al. 2003), which shows a double-peaked profile suggestive of orbital motion (Tacconi et al. 2006).

We detect SMM J04431+0210 in both F110W and F160W images, with a total extension of $\sim 1''.4$ in F160W where the S/N ratio is highest. The exceptional spatial resolution of our data allows us to distinguish for the first time two separate components in SMM J04431+0210, which are aligned in a near north-south direction and are labeled as sources A and B in the stamps shown in the third row of Figure 1. Component A consists of a bright compact nucleus surrounded by an extended envelope of diffuse light that is more extended towards the east, while component B appears to be an entirely diffuse, irregular structure, and is only marginally detected in the F110W image.

The only previous indication of the two-component nature of SMM J04431+0210 comes from the detection of a double-peaked CO(3–2) profile, which is centered at J2000 coordinates RA=04:43:7.24 and decl.=+02:10:23.8 and has blue- and red-shifted peaks separated by $0''.7 \pm 0''.3$ in a north-south direction (Tacconi et al. 2006). The CO(3–2) centroid position matches the location of the near-infrared emission within the combined uncertainties of our registration ($\pm 0''.4$) and the coordinates reported by Tacconi et al. (2006, $\pm 0''.4$), and falls roughly between components A and B, as indicated by the cross in Figure 1. Furthermore,

the separation between the peaks is consistent with the $0''.53$ distance that we measure between the centroids of components A and B along the declination axis. The detection of a double-peaked profile and the decomposition into two spatial components suggest that SMM J04431+0210 is an ongoing merger system.

SMM J14011+0252 is an $S(850\mu\text{m}) = 14.6 \pm 1.8$ mJy source detected by the SCUBA Lens Survey toward the cluster A1835, which causes a moderate amplification factor of 2.75 (Smail et al. 1997). This SMG is associated with a 1.4 GHz radio counterpart and a pair of optical/near-infrared sources at redshift $z = 2.56$ denoted J1 and J2, which show no evidence of AGN activity (Ivison et al. 2000; Fabian et al. 2000), thus suggesting that the enormous energy output of SMM J14011+0252 is caused by an ultraluminous starburst (Frayser et al. 1999). High-resolution optical and millimeter imaging revealed a complex morphology for J1 (Ivison et al. 2001) with a series of bright knots and a central concentration (J1c), identified as a foreground cluster member that is responsible for a modest additional magnification (factor $\sim 3 - 5$; Smail et al. 2005). The likely scenario here is that SMM J14011+0252 is a two-component system, in which J1 is a massive starburst with some bright clumps of relatively unobscured star formation induced by a dynamical interaction with companion J2. We adopt a magnification factor of 4.0 in calculating rest-frame quantities for J1, and a magnification of 3.5 for J2.

Our data for SMM J14011+0252 include the highest resolution infrared imaging of the galaxy obtained so far, and optical (F850LP) ACS imaging that surpasses in resolution the previously analyzed F702W/WFPC2 data. We are now able to study the system’s near-infrared morphology with the same detail that is possible in the optical. As shown in the fourth row of Figure 1, components J1 and J2 are clearly detected in bands F110W, F160W, and F850LP, but the substructures in J1 are more notable in F110W and F850LP, where the knots originally detected by Ivison et al. (2001) are more clearly defined. Before measuring magnitudes for J1 we remove J1c, which we model in the F850LP image with GALFIT assuming a Sérsic profile. The best fit is a profile with index $n = 1.12 \pm 0.05$ and effective radius $R_e = 0''.36 \pm 0''.02$, which leaves negative residuals of order 10% of the source’s flux at the center. These parameters are consistent with the model of Nesvabda et al. (2007). The oversubtraction becomes less important as the radius increases: it drops to $\sim 5\%$ at a radius of $0''.2$ and approaches zero at $\sim 0''.3$, so the induced error in the photometry of J1 is not significant. We then scale this model to the remaining bands by measuring the relative fluxes inside the effective radius and subtract the scaled versions. To illustrate our modeling of J1c, in the rightmost panel of Figure 1 we show the original image in band F850LP, and in the remaining panels we show the residual images in all filters.

SMM J16359+6612 is an intrinsically very faint SMG at $z = 2.516$ amplified by the core of the rich cluster A2218, which produces three images denoted A, B, and C (Kneib et al. 2004). The estimated magnification factors for each image are 14 ± 2 , 22 ± 2 , and 9 ± 2 respectively (Kneib et al. 2005). Optical and near-infrared data reveal a very red counterpart with two blue knots surrounding a red core (Kneib et al. 2004). CO(3–2), CO(4–3), CO(6–5), and CO(7–6) lines show a double-peaked profile, suggesting that the molecular gas traces a rotating disk or torus (Sheth et al. 2004; Kneib et al. 2005; Weiß et al. 2005).

Our F110W and F160W data for SMM J16359+6612 cover the locations of counterparts A and B; near-infrared and optical stamps for both images are shown in Figure 1. Counterpart B lies close to the edge of the NICMOS field in a rather noisy section of the image, but near-infrared/optical magnification-corrected magnitudes for sources A and B are consistent within errors (Table 3). Hence, for the stellar population analysis performed in Section 5 we use only the results obtained for counterpart A; the agreement in magnitudes measured in all bands gives us confidence that the analysis of image A is sufficient to understand the stellar population properties of the lensed SMG.

SMM J16368+4057 (N2 850.4; Scott et al. 2002) is a relatively bright unlensed submillimeter source ($S(850\mu\text{m}) = 8.2 \pm 1.7$ mJy) associated with a strong ($S(1.4\text{ GHz}) = 220\ \mu\text{Jy}$), compact radio source (Ivison et al. 2002). UV, optical, and millimeter spectroscopy provide evidence that SMM J16368+4057 is a massive, late-stage merger of at least two components, which has triggered a strong, obscured starburst and an AGN (Smail et al. 2003; Neri et al. 2003; Swinbank et al. 2005; Tacconi et al. 2008). Swinbank et al. (2005) identify three dynamically distinct components (denoted A, B, and C) and detect broad-line emission indicative of nuclear emission at the location of B and C, but do not reach a firm conclusion on which of them hosts the AGN.

We combine new F110W imaging of SMM J16368+4057 with the ACS F814W and NICMOS F160W data published by Swinbank et al. (2005) to study the properties of the starburst and AGN that likely power this source. Component A is not clearly distinguishable from B based on the optical/near-infrared imaging only, so we focus our analysis on B and C, shown in Figure 1, for which we define segmentation photometry apertures that are consistent with the $\text{H}\alpha$ velocity field contours in Swinbank et al. (2005). The magnitudes measured for sources B and C are given in Table 3. The F160W emission extends towards the north beyond the boundaries defined for components B and C, and traces an irregular tail that may be the result of tidal interactions. Component C becomes fainter as we move from the rest-frame optical to UV, but thanks to the addition of the F110W band we detect in component B a compact knot that is brighter in F814W than in F110W, and therefore

emits more strongly in the rest-frame UV. This nucleus suggests that the AGN is most likely located in component B, implying that the emission in component C is caused by star formation, and that the broad optical lines detected by Swinbank et al. (2005) in C are due to scattered emission (Smail et al. 2003).

We have removed component B’s point source in order to isolate and study the properties of the underlying starburst. As for SMM J02399–0136, we use GALFIT to generate the optical model from the F814W image, and then scale according to the central flux before subtracting from the infrared images.

4.2.2. *Single-component SMGs*

SMM J123549.44+621536.8 was included in the optical spectroscopic survey of Chapman et al. (2005), and it is been since found that it hosts a heavily obscured AGN component (Alexander et al. 2005; Takata et al. 2006), with double-peaked rest-frame optical emission lines that likely indicate a merger geometry or rotation along the slit. High-resolution millimeter imaging by Tacconi et al. (2006, 2008) revealed CO(3–2) and CO(5–6) lines with double-peaked profiles and gas kinematics that are interpreted as signs of a compact rotating merger remnant.

We detect SMM J123549.44+621536.8 in both F110W and F160W; it appears as a single central nucleus surrounded by a more irregular diffuse component. There are no signs of multiple nuclei, which suggests that the double-peaked profile seen in various spectral lines is likely caused by rotation rather than merging components. The F160W emission compact core has a diameter of $\sim 1''$, and the faint envelope has an extension of $\sim 1''.5$.

SMM J123707+621410 is an unlensed $S(850\,\mu\text{m}) = 4.7 \pm 1.5\,\text{mJy}$ source in the Hubble Deep Field North (Chapman et al. 2004, 2005), which has been resolved through high-resolution millimeter continuum imaging (Tacconi et al. 2006, 2008) into a double source with a separation of $\sim 2''.5$. One CO peak is coincident with a radio/optical/near-infrared source (Swinbank et al. 2004; Tacconi et al. 2008), while the second is only detected strongly in the radio continuum, with additional radio blobs seen around the (sub)millimeter source. These observations suggest a complex environment with several potential interacting sources, but we focus our analysis on the only component visible at near-infrared and optical wavelengths, for which we measure magnitudes in F160W and F110W, and in GOODS optical bands F606W (V), F775W (i), and F850LP (z). For band F435W (B), we can only estimate a magnitude limit. As seen in Figure 1, the source is small and compact, with a half-light radius of $\sim 3\,\text{kpc}$. Swinbank et al. (2004) distinguish in the optical (V, i, z) bands two nu-

clei separated by $\sim 0''.2$ that coincide with knots of $H\alpha$ emission, and that are therefore interpreted as two separate objects, but our data show that the F160W emission envelops both components, so they are probably just emission peaks in a single object with high but irregular absorption.

MM J154127+6616 is an unlensed source detected in a deep 1.2 mm MAMBO survey of A2125, for which Bertoldi et al. (2000) identified a radio and K -band counterpart, plus a faint arc seen in J and K imaging that appears to connect MM J154127+6616 with a brighter source located $\sim 4''$ to the southeast. MM J154127+6616 is not detected in our F110W image, so we can only constrain its magnitude. Considering a 3σ threshold and a $2''$ aperture, as in the previous limit reported by Bertoldi et al. (2000), we find that $F110W > 25.7$. In the F160W band, we detect an irregular source with magnitude $F160W = 23.65 \pm 0.05$. We also see traces of the arc reported by Bertoldi et al. (2000) in our F110W data and more clearly in the F160W image – starting at a distance of $\sim 2''.5$ SE of MM J154127+6616, beyond the region shown in Figure 1 – so we are presumably looking at a less-obscured structure at the same redshift.

SMM J16366+4105 (N2 850.2) is an unlensed source detected in the SCUBA 8 mJy survey of the ELAIS N2 field (Scott et al. 2002; Fox et al. 2002), with a strong radio counterpart and complex, multicomponent K -band emission (Ivison et al. 2002), but undetected in optical VRI bands and without identifiable AGN features (Chapman et al. 2005; Swinbank et al. 2004). Millimeter observations have revealed a double-peaked CO(3–2) line (Greve et al. 2005; Tacconi et al. 2006) and a large ($\sim 10^{10} M_\odot$) dynamical mass enclosed within a small (1.6 kpc) radius, which are interpreted as evidence of a compact merger remnant (Tacconi et al. 2008).

In our NICMOS data, we detect a F160W ~ 25 mag source that is close to the edge of the image and therefore has a slightly larger photometric error than do our other targets. As shown in Figure 1, this source is compact, with a Petrosian radius of 2.86 kpc in F160W, and it matches one of the K -band components and the radio source detected by Ivison et al. (2002). However, the source is undetected in the F110W and F814W bands, for which we derive 5σ AB magnitude lower limits of 26.68 and 28.27, respectively.

SMM J16371+4053 SMM J16371+4053 is an unlensed source detected in a 1.2 mm MAMBO survey of the ELAIS-N2 field (Greve et al. 2004) that lies at $z = 2.38$ as measured from optical (Chapman et al. 2005) and CO (Greve et al. 2005) emission lines. Near-infrared spectroscopy has revealed $H\beta$ and [O II] emission consistent with the presence of an AGN

(Takata et al. 2006), but detection of mid-infrared PAH features suggest that its bolometric luminosity is dominated by starburst activity. In this work, SMM J16371+4053 is detected and resolved in both near-IR bands and in the F775W optical band; it has a central bright compact nucleus surrounded by a diffuse, irregular component.

5. MORPHOLOGICAL ANALYSIS

To study the infrared morphologies of our galaxies, we calculated a set of non-parametric measurements that quantify their internal structure. The Gini coefficient (G) gives a quantitative measure of how unequally a galaxy’s light is distributed among its pixels (Abraham et al. 2003); it takes a minimum value of zero if the light is distributed uniformly among all the pixels, and a maximum of 1 if all the light is concentrated in one pixel. The concentration index (C ; Abraham et al. 1994) is the ratio of the flux within an inner aperture to the flux outside it and is a proxy for a galaxy’s bulge-to-disk ratio, while the asymmetry parameter (A) quantifies the degree to which the light of a galaxy is rotationally symmetric (Lotz et al. 2004). We also studied the second-order moment of the brightest pixels, M_{20} (Lotz et al. 2004), which depends on the spatial distribution of any bright nuclei, bars, or off-center concentrations. These parameters have the advantage of not requiring any assumptions about a galaxy’s light profile, so they can be applied to irregular or disturbed galaxies; here we wish to evaluate if they correlate with the presence or absence of multiple components in merger-like SMGs.

All morphological parameters were computed with the PyCA software (Menanteau et al. 2006), which implements the mathematical definitions detailed in the Appendix. To determine the aperture within which all statistics are calculated, PyCA takes as input a SExtractor segmentation image used to define the total galaxy region; for this purpose, we used the segmentation images generated from F160W images with minimum deblending settings. In this way, we can examine if possible components or clumps affect the calculated morphological parameters, even if they are initially selected within a unified structure, and we can make a coherent comparison between the results obtained for F110W and F160W data, since we select the same physical area in both filters. Following the analysis by Lotz et al. (2004) of noise effects on the calculation of G , M_{20} , and A , we require a minimum S/N of 5 to perform a morphological analysis, and we assume a systematic uncertainty of 10% in our measurements.

We measured morphological parameters for all targets in bands F110W and F160W, except for MM J154127+6616 and SMM J16366+4105, which were not analyzed in band F110W due to low S/N. For SMM J16359+6612, we know that both counterparts (A and

B) are highly lensed and geometrically distorted by the cluster’s gravitational potential, so parameters that depend on the source’s spatial distribution, like A , C , and M_{20} , are not meaningful. The individual measurements are presented in Table 4, and the full set of results is summarized in Figure 3.

The sources are generally compact, with a mean half-light radius of $\langle r_h \rangle = 3.4 \pm 0.3$ kpc in the F110W band and $\langle r_h \rangle = 3.6 \pm 0.2$ kpc in F160W. If we correct for gravitational magnification for those targets that are lensed by cluster potentials, the F110W and F160W source-plane radii are $\langle r_h \rangle = 2.5$ kpc and $\langle r_h \rangle = 2.7$ kpc, respectively. These results agree with recent work by Swinbank et al. (2010b), who measure r_h , G , and A in F160W and in the optical I band for a sample of 23 SMGs with redshifts in the range $z = 0.7 - 3.4$. Their sample includes one of our objects, SMM J16368+4057, for which they measure a F160W half-light radius of 3.4 ± 0.4 kpc, in excellent agreement with our result for the object’s half-light semi-major axis, $a_h = 3.44$ kpc. For the full sample, they obtain median sizes of 2.3 ± 0.3 kpc and 2.8 ± 0.4 kpc in the observed optical and near-infrared, respectively. Swinbank et al. (2010b) also calculate and analyze the morphological parameters of SMM J02399–0136 (L1/L2) for the F160W band using source-plane *HST* imaging derived from a gravitational lensing model, and obtain $r_h = 2.8 \pm 0.4$ kpc, $G = 0.88$, and $A = 0.30$. We measure a lensing-corrected half-light radius of $r_h = 2.52$ kpc, consistent within errors with their value. Swinbank et al. (2010b) obtain $G = 0.83$ and $A = 0.66$ for this system, but a direct comparison with our G and A is not conclusive due to possible differences in the regions used by the two studies.

The median Gini coefficient and asymmetry for our sample are $(G, A) = (0.79 \pm 0.17, 0.63 \pm 0.02)$ in F110W, and $(G, A) = (0.70 \pm 0.11, 0.51 \pm 0.01)$ in F160W. These parameters characterize the morphologies of our targets at rest wavelengths of 3211 ± 215 Å and 4584 ± 238 Å, respectively. Swinbank et al. (2010b) differ in the median values for their SMG sample and obtain $G = 0.56 \pm 0.02$ and $A = 0.27 \pm 0.03$ in the observed near-infrared, but since calculation of morphological parameters depends strongly on aperture and signal-to-noise, quantitative comparison between different datasets is not straightforward (Lisker 2008). We can still contrast different interpretations regarding the utility of morphological parameters as indicators of merger-like configurations. For example, Swinbank et al. (2010b) compared the morphologies of SMGs with those of UV/optically selected star-forming galaxies, and found that the mean sizes, asymmetries, and Gini coefficients agree within uncertainties. Their conclusion is that the rest-frame UV/optical morphological parameters of SMGs are not more likely to indicate major mergers than they do for more typical galaxies at the same redshifts, even if spectroscopy at other wavelengths does reveal complex kinematics or merging systems. In our sample, however, we obtain a larger spread in A than Swinbank et al. (2010b) and find that the values do correlate to some extent with the existence of multi-

ple nuclei or complex configurations, especially in F160W. In Section 4.2 we analyzed each source in detail and classified each as a multiple or single-component system based on the segmentation images produced by SExtractor, which thanks to the high spatial resolution of our images is capable of separating independent components separated by a few kiloparsecs. In all cases, the identification of multiple components is supported by previous interferometric evidence, which consistently reveals complex, merger-like dynamical structures. Thus, we classified five of our targets as multiple-component systems and five as single-nuclei, as indicated in the last column of Table 4. In parallel, we calculated morphological parameters for each target, and as shown in Figure 3, the only significant trend we find is that sources for which we identify multiple components (plotted as dots) have systematically larger asymmetries than single objects (plotted as triangles) in band F160W. The median values are $A_M = 0.65 \pm 0.01$ and $A_S = 0.38 \pm 0.01$ for multiple and single-component systems respectively, and are plotted as open symbols in the middle-right panel of Figure 3. The only outlier from this trend is MMJ154127+6616, which has a high asymmetry despite being included in the single-component group; this object’s high value for A is explained by its unusual irregular, diffuse appearance. The trend of increased A for merger-like systems does not hold for band F110W, but at shorter wavelengths the asymmetry tends to increase for all objects, and the effect of multiple components may be masked by the existence of brighter knots of star formation or structured obscuration. For M_{20} and C , there are no clear differences in the measured values between the two source groups in any filter.

We believe that our ability to detect a correlation between A and probable merger-like configurations owes mainly to the homogeneity of our sample. Our targets span a narrow range of redshifts, with $z = 2.2 - 2.8$, so observations in band F160W correspond to similar rest-frame wavelengths for all objects. However, in the sample of Swinbank et al. (2010b), a significant number of objects lie at $z < 2$ and there is a much larger spread in redshift; F160W imaging consequently reflects a mixture of rest-frame morphologies, with 40% of the sample being observed at longer rest wavelengths than the average for our targets. By comparing F110W and F160W observed morphologies, we find that G and A tend to decrease as we move to redder bands, where dust obscuration is less structured. According to our analysis, we would expect an object with complex, merging morphology to have at least higher asymmetry than a single-component system, but this effect could be partially compensated if the multi-component object is actually being observed at a redder rest wavelength. Therefore, the A versus multiplicity trend seen in our sample could be blurred if the target selection is not homogeneous in terms of redshift, which explains the different assessments of morphological parameters as indicators of merger likelihood from this work and Swinbank et al. (2010b). Although the Swinbank et al. (2010b) sample includes SMGs at lower redshifts, a lower redshift is no guarantee that an object is more evolved than ob-

jects at $z = 2.2 - 2.8$, so we believe that our differing morphological measurements are not reflecting an evolutionary trend. As a further indication of the difference between samples, only two objects in the Swinbank et al. (2010b) sample would definitely have matched our selection criteria. However, our targets’ mean redshift ($\langle z \rangle = 2.1$) is closer to the peak of the SMG redshift distribution (Chapman et al. 2005), so our conclusions may be at least representative for the population.

6. Stellar masses

For SMGs with data and significant detections in three or more bands, we can compare the observed magnitudes with those expected for evolved stellar populations of different ages and star formation histories (SFHs) at the same redshift, and in this way study their physical properties. We used the GALAXEV library of SPS models and the `csp_galaxev` code (Bruzual & Charlot 2003, BC2003) to compute the spectra of evolved stellar populations with solar metallicity and a Chabrier (2003) IMF at various ages for an assortment of SFHs, including reddening. For the SFH, we adopted an exponentially declining function with an e -folding timescale τ in the range $\tau = 0.1 - 5$ Gyr to cover a representative set of models. For each model, we computed the evolved spectra at ages between 0 and 5 Gyr with uniform spacing of 0.1 Gyr, and included the effect of dust attenuation by applying a Calzetti et al. (2000) extinction (A_V) curve, with $A_V = 0.001$ (\sim no extinction) to $A_V = 5$ in steps of $\Delta A_V = 0.25$.

With the exceptional spatial resolution provided by *HST*, we can characterize the components in multiple systems *individually*, and thus study the stellar properties of the galaxies that build up SMGs. From our analysis of *HST* near-infrared imaging, we have identified multiple components in four SMG systems (SMM J02399–0136, SMM J04431+0210, SMM J14011+0252, and SMM J16368+4057). There is evidence from previous millimeter interferometry that SMM J123707+621410 is also a complex system with several potential interacting components (Tacconi et al. 2006, 2008), but only one is detected in the near-infrared/optical, so for the sake of our stellar population analysis we treat it as a single SMG. For SPS modeling of multiple-component systems, we do not take into account previous ground-based data, since we are specifically interested in studying them at *HST* resolution, where components can be resolved. However, for analysis of the six remaining SMGs where we identify single stellar components (SMM J123549.44+621536.8, SMM J123707+621410, SMM J154127+6616, SMM J16359+6612, SMM J16366+4105, and SMM J16371+4053), we can improve our stellar population modeling by including results from previous authors. In the analysis of SMM J123549.44+621536.8, SMM J123707+621410, SMM J16366+4105, and

SMM J16371+4053, we include IRAC photometry from Hainline et al. (2009); in the case of SMM J123549.44+621536.8, and SMM J123707+621410 we consider as well the optical magnitudes reported in Borys et al. (2005). For MM J154127+6616, there are no additional measurements in the rest-frame UV/optical.

For each object with multiwavelength photometry, χ^2 minimization can be used to find the best-fitting stellar population model. However, for a limited number of photometric points, there will be a broad set of models with different star formation timescales, ages, and reddenings that provide similarly good fits, as demonstrated for instance in Hainline et al. (2011). To illustrate this point in the context of our data, we show in Figure 2 synthetic color-color plots for our set of stellar population models at the redshift of SMM J02399–0136 ($z = 2.81$), and we also plot the observed photometry for each component in the SMM J02399–0136 system, as well as associated error ellipses with semi-major and semi-minor axes $a = \sigma_1$ and $b = \sigma_2$, for σ_1 and σ_2 the photometric errors for the two colors in the plot as derived from Table 3. We find that for L2 and L1sb there are numerous SPS models that reproduce the observed colors, while for L1N there are various evolved stellar populations that simultaneously fit all but the F475W observed magnitude, which we attribute to our simple treatment of dust attenuation. The `csp_galavex` code applies the two-component model of Charlot & Fall (2000) that accounts for attenuation due to dust in the outer envelopes of the dense clouds where stars are formed and in diffuse cirrus clouds in the interstellar medium. It is likely, however, that the dust distribution in SMGs is patchy and inhomogeneous (Chapman et al. 2004), introducing complex reddening effects. Detailed modeling of a clumpy dust geometry would necessarily introduce a large number of free parameters and degeneracies, and thus a significantly larger number of data points would be required for a meaningful result.

With the current dust treatment, we can find compatible SPS models for all objects in our sample if we relax our matching criteria and require that the predicted magnitudes are within 3σ of the observed magnitudes in all available bands. The set of compatible SPS models spans wide ranges in age, timescale τ , and extinction A_V , so we are therefore unable to reliably estimate these parameters, but we can constraint stellar masses, which are more narrowly distributed, with a typical dispersion $\Delta \log M_* = \pm 0.1$. To properly account for the uncertainties due to age, extinction, and SFH degeneracies, we used Hyperzmass (Pozzetti et al. 2007) to calculate the stellar masses predicted by all selected models, and we adopt the mean and dispersion of the resulting distribution as our final value and uncertainty in M_* . With this approach, we estimated stellar masses for all SMGs and SMG components except MM J154127+6616, which we detect only in F160W and has no additional optical/near-infrared photometry in the literature. For SMM J04431+0210, we only have F110W and F160W magnitudes for both components, but since these filters bracket the

Balmer/4000 Å break, they provide an effective constraint on the rest-frame SEDs, so we can still estimate stellar masses for SMM J04431+0210A and SMM J04431+0210B, albeit with moderately larger uncertainties. Our results are summarized in Table 5, where we report our stellar mass estimates and mass ratios for multi-component systems.

Previous analyses of SMG stellar populations have produced mean masses that differ by factors up to ~ 10 . Hainline et al. (2011) subtracted the near-IR continuum excess contributed by AGNs and obtained a median $\log(M_*/M_\odot) \sim 10.8$, while other studies also based on SED fitting suggest higher masses in the range $\log(M_*/M_\odot) = 11.4 - 11.8$ (Borys et al. 2005; Dye et al. 2008; Michalowski et al. 2010). The latter estimates support the scenario proposed by Davé et al. (2010), who studied the nature of rapidly star-forming galaxies at $z = 2$ in cosmological hydrodynamic simulations and concluded that SMGs may not be scaled up versions of local major mergers seen as ULIRGs, but can be explained instead as super-sized versions of ordinary star-forming galaxies fed by infalling gas-rich satellites. This cold accretion model, however, implies stellar masses in the range $\log(M_*/M_\odot) \sim 11 - 12$, so confirmation of lower masses like those estimated by Hainline et al. (2011) would undermine this interpretation.

We have estimated the total stellar masses of nine SMGs, four of which are separated into two or more interacting components. If we add up these individual concentrations and consider the total mass of each SMG system, we obtain values in the range $\log(M_*/M_\odot) \sim 9.6 - 11.8$, with a sample mean of $\log(M_*/M_\odot) = 10.9 \pm 0.2$. We have four objects in common with Hainline et al. (2011) and Michalowski et al. (2010) (SMM J123549.44+621536.8, SMM J123707+621410, SMM J16366+4105, and SMM J16371+4053); for the first two of these we estimate masses that are a factor $\sim 4 - 8$ lower than those of Michalowski et al. (2010) (even after scaling our values to their Salpeter IMF), but within a factor ~ 2 of the results of Hainline et al. (2011). For SMM J16366+4105 and SMM J16371+4053, however, our mass estimates for single-component SMGs are in good agreement with those of Michalowski et al. (2010). In general, we find that our mean stellar mass is consistent with that of Hainline et al. (2011), but individual masses span the range of values from the more modest measurements of Hainline et al. (2011) to the higher predictions of Davé et al. (2010), consistent with both formation channels – major mergers and cold accretion – playing a role in the birth of SMGs.

Aside from stellar masses, we can also find indications of these two formation mechanisms imprinted in the morphologies of the SMGs in our sample. First, we find that half of our sample presents high asymmetries that correlate with complex, multi-component morphologies that may be attributed to mergers or interacting systems- consistent with previous spectroscopic studies that detect complex dynamical structures. For multiple systems, we

are able to estimate stellar masses for *each* component and therefore their mass ratios. We find, for example, that for binary sources like SMM J04431+0210 and SMM J16368+4057 with moderate total masses ($< 10^{11} M_{\odot}$), the proportions are respectively $\sim 3:1$ or close to unity, similar to the ratios observed by Dasyra et al. (2006) for local ULIRGs. This result is consistent with that of Engel et al. (2010), who measure dynamical mass ratios for four binary SMGs and broadly conclude that most SMGs are major mergers. However, in the massive system SMM J02399–0136, the mass ratios that we have now measured between the central concentration (L1sb) and its companions (L1N and L2)—not available to Engel et al. (2010)—are significantly larger ($\sim 50:1$ and $\sim 126:1$, respectively), suggesting that the SMG starburst is taking place in a system that may be undergoing a minor merger. We also find that some of the most massive objects like MM J154127+6616, SMM J123707+621410, and SMM J16371+4053 show no distinct mass concentrations or evidence of merging nuclei, and have optical rest-frame morphologies more consistent with the simulated rapidly star-forming galaxies at $z = 2$ in the work of Davé et al. (2010). We conclude that depending on which extreme of the SMG mass range we are looking at, there is observational evidence to support either the major merger or the cold accretion scenario, so it is entirely possible that we are studying a heterogeneous population in which different formation mechanisms are involved.

7. CONCLUSIONS

We have presented *HST* NICMOS and WFC3 near-infrared imaging in bands F110W ($\sim J$) and F160W ($\sim H$) for a sample of 10 SMGs with redshifts in the range $z = 2.2 - 2.8$, which we have combined with existing optical ACS data in order to study their morphologies, stellar populations, and stellar masses. Out of our sample, eight targets were detected in both NICMOS bands, and two were detected only in F160W. The sample was deliberately selected so that each object had a CO or PAH-confirmed redshift that put the Balmer/4000 Å break between the F110W and F160W bands; all objects are brighter in the latter band, so we used it as the reference detection frame.

To study the possible multi-component, merger-like nature of our targets, we took advantage of the maximum deblending option in SExtractor to assess whether each system could be resolved into two or more stellar structures coalescing to form a massive SMG. Through this analysis, and with the support of previous dynamical evidence, we were able to classify four of our targets (SMM J02399–0136, SMM J04431+0210, SMM J14011+0252, and SMM J16366+4105) as multi-nuclei systems at different merger stages, and measured magnitudes for individual components. Previous CO data show that SMM J123707+621410 is also an early-stage merger system with only one component visible in the rest-frame op-

tical (Tacconi et al. 2008). Thus, five objects in our sample show rest-frame optical and/or molecular gas morphologies that are consistent with ongoing mergers. The high resolution and long wavelength of our *HST* imaging have allowed us to characterize our targets with greater confidence than has been possible in the past: we have newly identified the large central mass concentration underlying the bright AGN in SMM J02399–0136, the binary merger of SMM J04431+0210, and the location of the optically bright AGN in SMM J16368+4057. With the advent of high-resolution millimeter/submillimeter observations with ALMA, it will be possible to discern merger-like configurations and identify components in samples selected from the high-redshift end of the SMG population, as shown in the study of a massive starburst at $z = 4.7$ by Wagg et al. (2012) and Carilli et al. (2013).

In addition to this photometric analysis, we have also measured the mean source sizes and studied the morphologies of our SMG sample. We calculated the asymmetry (A), Gini coefficient (G), second-order moment of brightest pixels (M_{20}), and concentration (C) in bands F110W and F160W, in order to study possible morphological evolution with wavelength, and to determine whether these parameters are useful as indicators of mergers. The observed circularized radii are $\langle r_h \rangle = 3.4 \pm 0.3$ kpc for F110W and $\langle r_h \rangle = 3.6 \pm 0.2$ kpc for F160W; this last result and results for individual objects are comparable to those of earlier studies (e.g., Swinbank et al. 2010b; Targett et al. 2011). We also find that parameters G , C and M_{20} do not show any clear evolution between bands F110W and F160W, and do not correlate with the presence or absence of multiple components. However, A is higher in F110W than in F160W; the mean values are $A_{\text{F110W}} = 0.63 \pm 0.02$ and $A_{\text{F160W}} = 0.51 \pm 0.01$, respectively. This trend is consistent with deeper, more structured obscuration and more concentrated star activity in bluer bands, and is also in agreement with previous measurements by Swinbank et al. (2010b). When we compare the mean A for the set of objects for which we identified multiple components with the mean values for single-nucleus SMGs, we find that in band F160W, A is higher for multiple systems. This trend between A and multiplicity indicates that A is a useful indicator of merging configurations, with the caveat that the sample under analysis must be homogeneously selected in terms of redshift for the trend to avoid being blurred out. Previous work by Swinbank et al. (2010b) concluded that the asymmetry of SMGs was comparable to that of UV-selected galaxies at the same epoch and therefore not a good reflection of their merger-like morphologies, but we believe that in this case the expected increase in asymmetry with morphological complexity may have been masked by the sample’s larger spread in redshift.

We have carried out a SPS analysis for all objects detected in at least two *HST* near-infrared bands, using as well optical *HST* archive data when available, plus IRAC and/or ground based optical/near-infrared measurements for single-component systems. We find that satisfactory SPS models span a wide range of ages and extinctions, so we are not able

to determine the SFH or a galaxy’s dust content based on the available data. However, we are able to constrain stellar masses for nine SMGs, and in four multiple systems we obtain stellar masses for each of the components that are likely merging to build up a larger SMG. Determination of SMG stellar masses allows us to assess the predictions of the cold accretion scenario (Davé et al. 2010), which has been proposed as an alternative to the typical major-merger formation model. The former predicts number densities and clustering that match current observations, but it requires stellar masses in the range $\log(M_*/M_\odot) \sim 11 - 12$, and would be less preferred if more modest estimates like those of Hainline et al. (2011) are correct. For our sample, we find that if we consider the total combined masses in each SMG system, our estimates range from $\log(M_*/M_\odot) \sim 9.6$ to ~ 11.8 , with a mean of $\log(M_*/M_\odot) = 10.9 \pm 0.2$. These values suggest that both mechanisms may be operating, and a more detailed analysis of stellar masses versus morphologies for individual objects supports this view. Either the most massive systems show no evidence of multiple concentrations or merger-like morphologies, resembling the simulated examples of Davé et al. (2010), or they can be separated into two or more merging components whose high mass ratio does not agree with the “major merger” definition but more likely suggests accretion of small companions. On the other hand, less-massive objects with clear merging morphologies do have mass ratios comparable to those observed for local ULIRGs, and could therefore be interpreted as scaled-up versions of that local population. We speculate then that both the major merger and the cold accretion mechanisms have contributed to the formation of the SMG population, but on opposite extremes of the observed stellar mass range.

The authors thank Galina Soutchkova and Jason Kalirai for their help in coordinating the *HST* observations, Saquib Ahmed for his contributions to the early stages of our analysis of the data, and an anonymous referee for comments that helped improve the paper. Support for this project was provided by NASA grant HST-GO-11143.01-A. P. Aguirre acknowledges support from the FONDAPE Center for Astrophysics 15010003, BASAL CATA Center for Astrophysics and Associated Technologies, the Chilean National Committee for Research in Science and Technology (CONICYT), MECESUP, and Universidad Andres Bello Regular Project DI-05-11/R.

A. CALCULATION OF MORPHOLOGICAL PARAMETERS

For clarity and ease of comparison with other work, we review here our definitions and practices for measurement of morphological parameters.

A.1. Gini Coefficient (G)

We calculated G according to the formulas in Glasser (1962). This definition depends heavily on the selection of pixels that belong to a galaxy; we used all pixels inside an elliptical aperture with semi-major axis $R_p = 1.5 \cdot r_p$, where r_p is the Petrosian (1976) radius at which the ratio of the surface brightness measured locally over the surface brightness averaged across the enclosed region is equal to a fixed number $\eta = \frac{\mu(r_p)}{\mu(r < r_p)}$, in this work set to 0.2. The elliptical aperture axial ratio was obtained by dividing the effective major and minor radii measured by SExtractor, and to characterize the source size we measured the *half-light* major (a_h) and minor (b_h) axes, defined as the dimensions of the ellipse that encloses half of the flux inside the Petrosian radius. For a better representation of the sizes of galaxies that are geometrically distorted by gravitational lensing, we then calculated the circularized radius $r_h = \sqrt{a_h \cdot b_h}$, which is not dominated by global cluster shear and scales as the square root of the magnification factor μ . The final elliptical apertures were carefully checked to ensure that there was no contamination from other sources in the calculation of morphological parameters.

A.2. Concentration Parameter (C)

The concentration parameter C is generally defined as the integrated flux inside an inner isophote or radius αR divided by the flux inside R , for some $\alpha < 1$ (Abraham et al. 1994). Following Menanteau et al. (2006) we used $\alpha = 0.3$, so that C is computed as:

$$C = f(0.3R)/f(R) , \tag{A1}$$

with $f(r) = 2\pi \int_0^R I(r) dr$. The distance R was defined as $R = 1.5 \cdot r_p$.

A.3. Asymmetry (A)

The asymmetry parameter A measures the fractional difference between the original image and the same image rotated by 180° around its centroid, corrected for variations in the image background. The pivot point for rotation is defined as the position that yields minimum asymmetry (Conselice et al. 2000). To find it, we used the galaxy’s luminosity centroid as a first guess, calculated A , and then repeated using as centers the eight surrounding points in a 3×3 grid, with a grid spacing of 0.1 pixels. If A was minimized at the grid center, we chose this point as the rotation center; otherwise the procedure was repeated

for a new grid centered on the point where the asymmetry was lowest, and continued until a minimum was found.

The effects of correlated noise were removed by performing the same asymmetry measurement on a portion of neighboring blank sky. The sky asymmetry was minimized and scaled by the size of the object relative to that of the blank region, normalized by the object's total flux and subtracted from the value measured for the galaxy, so that the final formula used to compute A resulted in

$$A = \min \left(\frac{\sum |I_0 - I_R|}{\sum I_0} \right) - \min \left(\frac{\sum |B_0 - B_R|}{\sum I_0} \right) \quad (\text{A2})$$

where I_0 is the original source image, B_0 represents the blank sky pixels, and I_R and B_R are the corresponding images rotated by 180° .

A.4. Second-order Moment of Light of the Brightest 20% of the Galaxy's Pixels (M_{20})

The total second-order moment of light corresponds to the sum of all pixel fluxes multiplied by their squared distances to the centroid, such that $M_{\text{tot}} = \sum_{i=1}^n M_i = \sum_{i=1}^n f_i [(x_i - x_c)^2 + (y_i - y_c)^2]$; high values reflect the existence of bright nuclei away from the galaxy's centroid or extended light distributions like bars or spiral arms (Lotz et al. 2004). Based on this definition, M_{20} was calculated as

$$M_{20} = \log_{10} \left(\frac{\sum_i M_i}{M_{\text{tot}}} \right), \quad \text{while} \quad \sum_i f_i < 0.2 \cdot f_{\text{tot}} \quad (\text{A3})$$

REFERENCES

- Abraham, R. G., Valdes, F., Yee, H. K., & van den Bergh, S. 1994, ApJ, 432, 75
- Abraham, R. G., van den Bergh, S. & Nair, P., 2003, ApJ, 588, 218
- Adelberger, K. L., Steidel, C. C., Pettini, M., et al. 2005, ApJ, 619, 697
- Alexander, D. M., Bauer, F. E., Chapman, S.C., et al. 2005, ApJ, 632, 736
- Baugh, C. M., Lacey, C. G., Frenk, C. S., et al. 2005, MNRAS, 356, 1191
- Bautz, M. W., Malm, M. R., Baganoff, F. K., et al. 2000, ApJ, 543, L119

- Behroozi, P.S., Conroy, C. & Wechsler, R.H., 2010, *ApJ*, 717, 379
- Bertin, E. & Arnouts, S. 1996, *A&A*, 117, 393
- Bertoldi, F., Carilli, C. L., Menten, K. M., et al. 2000, *A&A*, 360, 92
- Blain, A. W., Smail, I., Ivison, R. J., Kneib, J.-P., & Frayer, D. T. 2002, *Physics Reports*, 369, 111
- Bolzonella, M., Miralles, J.-M., & Pelló, R. 2000, *A&A*, 363, 476
- Borys, C., Smail, I., Chapman, S. C., et al. 2005, *ApJ*, 635, 853
- Bruzual, G. & Charlot, S. 2003, *MNRAS*, 344, 1000
- Bundy, K., Ellis, R., Conselice, C., et al. 2006, *ApJ*, 651, 120
- Bushouse, H., MacKenty, J., Skinner, C., & Stobie, E. 1997 in *ASP Conf. Ser. 125, Astronomical Data Analysis Software and Systems VI*, ed. G. Hunt & H.E. Payne (San Francisco, CA: ASP), 439
- Bushouse, H., & Simon, B. 1994, in *ASP Conf. Ser. 61, Astronomical Data Analysis Software and Systems III*, ed. D. R. Crabtree, R. J. Hanisch, & J. Barnes (San Francisco, CA: ASP), 339
- Calzetti, D., Armus, L., Bohlin, R. C., et al. 2000, *ApJ*, 533, 682
- Capak, P., Cowie, L. L., Hu, E. M., et al. 2004, *AJ*, 127, 180
- Carilli, C., Riechers, D., Walter, F. et al. 2013, *ApJ*, 763, 120
- Casertano, S., de Mello, D., Dickinson, M., et al. 2000, *AJ*, 120, 2747
- Chabrier, G., 2003, *PASP*, 115, 763
- Chapman, S. C., Blain, A. W., Smail, I., & Ivison, R. J. 2005, *ApJ*, 622, 772
- Chapman, S. C., Smail, I., Windhorst, R., Muxlow, T., & Ivison, R. J. 2004, *ApJ*, 611, 732
- Chapman, S. C., Windhorst, R., Odewahn, S., Yan, H., & Conselice, C. 2003, *ApJ*, 599, 92
- Charlot, S. & Fall, S.M., 2000, *ApJ*, 539, 718
- Cimatti, A., Daddi, E., & Renzini, A. 2006, *A&A*, 453, L29
- Conselice, C. J., Bershad, M. A. & Gallagher, J. S. III 2000, *A&A*, 354, L21

- Cowie, L. L., Songaila, A., Hu, E. M., & Cohen, J. G. 1996, *AJ*, 112, 839
- Dasyra, K. M., Tacconi, L. J., Davies, R. I., et al. 2006, *ApJ*, 638, 745
- Davé, R., Finlator, K., Oppenheimer, B. D., et al. 2010, *MNRAS*, 404, 1355
- Dekel, A. & Birnboim, Y. 2006, *MNRAS*, 368, 2
- De Lucia, G., Springel, V., White, S. D. M., et al. 2006, *MNRAS*, 366, 499
- Dye, S., Eales, S. A., Aretxaga, I., et al. 2008, *MNRAS*, 386, 1107
- Engel, H., Tacconi, L. J., Davies, R. I., et al. 2010, *ApJ*, 724, 233
- Fabian, A. C., Smail, I., Iwasawa, K., et al. 2000, *MNRAS*, 315, L8
- Ford, H. C., Bartko, F., Bely, P. Y., et al. 1998, *Proc. SPIE*, 3356, 234
- Fox, M. J., Efstathiou, A., Rowan-Robinson, M., et al. 2002, *MNRAS*, 331, 839
- Frayer, D. T., Armus, L., Scoville, N. Z., et al. 2003, *AJ*, 126, 73
- Frayer, D. T., Harris, A. I., Baker, A. J. et al. 2011, *ApJ*, 726, L22
- Frayer, D. T., Ivison, R. J., Scoville, N. Z., et al. 1998, *ApJL*, 506, L7
- Frayer, D. T., Ivison, R. J., Scoville, N. Z., et al. 1999, *ApJL*, 514, L13
- Frayer, D. T., Reddy, N. A., Armus, L., et al. 2004, *AJ*, 127, 728
- Genzel, R., Baker, A. J., Tacconi, L. J., et al. 2003, *ApJ*, 584, 633
- Gialalisco, M., Dickinson, M., Ferguson, H. C., et al. 2004, *ApJL*, 600, L103
- Glasser, G. J. 1962, *J. Am. Stat. Assoc.*, 57, 648
- Goldader, J. D., Meurer, G., Heckman, T.M., et al. 2002, *ApJ*, 568, 651
- Greve, T. R., Bertoldi, F., Smail, I., et al. 2005, *MNRAS*, 359, 1165
- Greve, T. R., Ivison, R. J., Bertoldi, F. et al. 2004, *MNRAS*, 354, 779
- Hainline, L., Blain, A. W., Smail, I., et al. 2009, *ApJ*, 699, 1610
- Hainline, L., Blain, A. W., Smail, I., et al. 2011, *ApJ*, 740, 96
- Harris, A. I., Baker, A. J., Frayer, D.T., et al. 2012, *ApJ*, 752, 152

- Hayward, C. C., Kereš, D., Jonsson, P., et al. 2011, *ApJ*, 743, 159
- Hildebrandt, H., Pierlorz, J., Erben, T. et al., 2009, *A&A*, 498, 725
- Iverson, R., Smail, I., Le Borgne, J.-F., et al. 1998, *MNRAS*, 298, 583
- Iverson, R. J., Greve, T. R., Smail, I., et al. 2002, *MNRAS*, 337, 1
- Iverson, R. J., Smail, I., Barger, A. J., et al. 2000, *MNRAS*, 315, 209
- Iverson, R. J., Smail, I., Frayer, D. T., Kneib, J.-P., & Blain, A. W. 2001, *ApJL*, 561, L45
- Iverson, R. J., Smail, I., Papadopoulos, P. P., et al. 2010, *MNRAS*, 404, 198
- Kannappan, S. J., Guie, J. M., & Baker, A. J. 2009, *AJ*, 138, 579
- Kereš, D., Katz, N., Fardal, M., Davé, R. & Weinberg, D. H. 2009, *MNRAS*, 395, 160
- Kereš, D., Katz, N., Weinberg, D. H., & Davé, R. 2005, *MNRAS*, 363, 2
- Kimble, R. A., MacKenty, J. W., O’Connell, R. W., & Townsend, J. A. 2008, *Proc. SPIE*, 7010, 70101E
- Kneib, J.P., Neri, R., Smail, I., et al. 2005, *A&A*, 434, 819
- Kneib, J.P., van der Werf, P., Knudsen, K., et al. 2004, *MNRAS*, 349, 1211
- Koekemoer, A., Fruchter, A., Hook, R., & Hack, W. 2003, in *HST Calibration Workshop, Hubble after the Installation of the ACS and the NICMOS Cooling System*, ed. S. Arribas, A. Koekemoer, & B. Whitmore (Baltimore, MD: STScI), 337
- Kovács, A., Chapman, S. C., Dowell, C. D., et al. 2006, *ApJ*, 650, 592
- Kriek, M., van Dokkum, P. G., Franx, M., et al. 2006. *ApJ*, 645, 44
- Lisker, T. 2008, *ApJ*, 179, 319
- Lotz, J. M., Primack, J. & Madau, P. 2004, *AJ*, 128, 163
- Lupu, R. E., Scott, K. S., Aguirre, J. E., et al. 2012, *ApJ*, 757, 135
- Lutz, D., Valiante, E., Sturm, E., et al. 2005, *ApJL*, 625, L83
- Marconi, A., Risaliti, G., Gilli, R., et al. 2004, *MNRAS*, 351, 169
- Menanteau, F., Ford, H. C., Illingworth, G. D., et al., 2004, *ApJ*, 612, 202

- Menanteau, F., Ford, H. C., Motta, V. et al., 2006, *AJ*, 131, 208
- Menéndez-Delmestre, K., Blain, A. W., Alexander, D. M., et al. 2007, *ApJ*, 655, 65
- Michalowski, M., Hjorth, J. & Watson, D. 2010 *A&A*, 514, A67
- Mo, H. J. & White, S. D. M. 2002, *MNRAS*, 336, 112
- Moster, B.P., Naab, T. & White, S.D., 2013, *MNRAS*, 428, 3121
- Moster, B.P., Somerville, R., Maubetsch, C. et al., 2010, *ApJ*, 710, 903
- Motohara, K., Takata, T., Iwamuro, F., et al. 2005, *AJ*, 129, 53
- Neri, R., Genzel. R., Ivison, R. J., et al. 2003, *ApJL*, 597, L113
- Nesvabda, N. P. H., Lehnert, M. D., Genzel, R., et al. 2007, *ApJ*, 657, 725
- Ouchi, M., Shimasaku, K., Okamura, S., et al. 2004, *ApJ*, 611, 685
- Papovich, C., Dickinson, M., & Ferguson, H. C. 2001, *ApJ*, 559, 620
- Peng, C., Ho, L. C., Impey, C. D. & Rix, H.-W. 2002, *AJ*, 124, 266
- Petro, L. & Baggett, L. 2009, “WFC3 Space Telescope Analysis Newsletter September 2009”
- Petrosian, V., 1976, *ApJL*, 209, L1
- Pier, J.R., Munn, J., Hindsley, R.B., et al. 2003, *AJ*, 125, 1559
- Poggianti, B. M. & Barbaro, G. 1997, *A&A*, 325, 1025
- Pope, A., Chary, R. R., Alexander, D. M., et al. 2008, *ApJ*, 675, 1171
- Pozzetti, L., Bolzonella, M., Lamareille, F., et al. 2007, *A&A*, 474, 443
- Quijano, K., et al. 2009, “WFC3 Mini-Data Handbook,” Version 1.0 (Baltimore, MD: STScI)
- Salpeter, E. E. 1955, *ApJ*, 121, 161
- Scott, S. E., Fox., M. J., Dunlop, J. S., et al., 2002, *MNRAS*, 331, 817
- Shankar, F., Lapi, A., Salucci, P., De Zotti, G. & Danese, L., 2006, *ApJ*, 634, 14
- Sheth, K., Blain, A. W., Kneib, J.-P., et al., 2004, *ApJL*, 614, L5
- Smail, I., Chapman, S. C., Blain, A. W., & Ivison, R. J. 2004, *ApJ*, 616, 71

- Smail, I., Chapman, S.C., Ivison, R. J., et al. 2003, MNRAS, 342, 1185
- Smail, I., Ivison, R. J., & Blain, A. W. 1997, ApJL, 490, L5
- Smail, I., Ivison, R. J., Blain, A. W., & Kneib, J.P. 2002, MNRAS, 331, 495
- Smail, I., Ivison, R. J., Kneib, J. P., et al., 1999, MNRAS, 308, 1061
- Smail, I., Smith, G. P., & Ivison, R. J. 2005, ApJ, 631, 121
- Somerville, R., 2009, MNRAS, 399, 1988
- Somerville, R., Hopkins, P.F., Cox, T.J., Robertson, B.E., Hernquist, L., 2008, MNRAS, 391, 481
- Swinbank, A. M., Smail, I., Bower, R. G., et al., 2005, MNRAS, 359, 401
- Swinbank, A. M., Smail, I., Chapman, et al., 2004, ApJ, 617, 64
- Swinbank, A. M., Smail, I., Chapman, S. C. et al. 2010, Nature, 464, 733
- Swinbank, A. M., Smail, I., Chapman, S. C. et al. 2010, MNRAS, 405, 234
- Swinbank, M., Chapman, S.C., Smail, I. et al., 2006, MNRAS,
- Tacconi, L. J., Neri, R., Chapman, S. C., et al. 2006, ApJ, 640, 228
- Tacconi, L. J., Genzel, R., Smail, I., et al., 2008, ApJ, 680, 246, 371, 465
- Takata, T., Sekiguchi, K. Smail, I., et al.. 2006, ApJ, 651, 713
- Targett, T., Dunlop, J. S., McLure, R. J., et al. 2011, MNRAS, 412, 295
- Thatte, D., Dahlen, T., et al. 2009, “NICMOS Data Handbook, version 8.0” (Baltimore: STScI)
- Thomas, D., Maraston, C., Bender, R., & Mendes de Oliveira, C. 2005, ApJ, 621, 673
- Thompson, R. I., Rieke, M., Schneider, G., Hines, D. C., & Corbin, M. R. 1998, ApJL, 492, L95
- Trentham, N., Kormendy, J., & Sanders, D. B. 1999, AJ, 117, 2152
- Valiante, E., Lutz, D., Sturm, E., et al. 2007, ApJ, 660, 1060
- Vernet J., & Cimatti A., 2001, A&A, 380, 409

- Villar-Martín, M., Binette L., & Fosbury R. A. E., 1999, A&A, 346, 7
- Wagg, J., Wiklind, T., Carilli, C. et al. 2012, ApJ, 752, 30
- Wake, D.A., Whitaker, K.E., Labbé, I. et al., 2011, ApJ, 728, 46
- Wang, L., Farrah, D., Oliver, S.J. et al., 2012, arXiv:1203.5828
- Wei A., Downes, W. F. & Henkel, C. 2005, A&A, 429, L25
- Yang, X., Mo, H.J., van den Bosch, F.C., Zhang, Y. & Han, J., 2012, ApJ, 752, 41

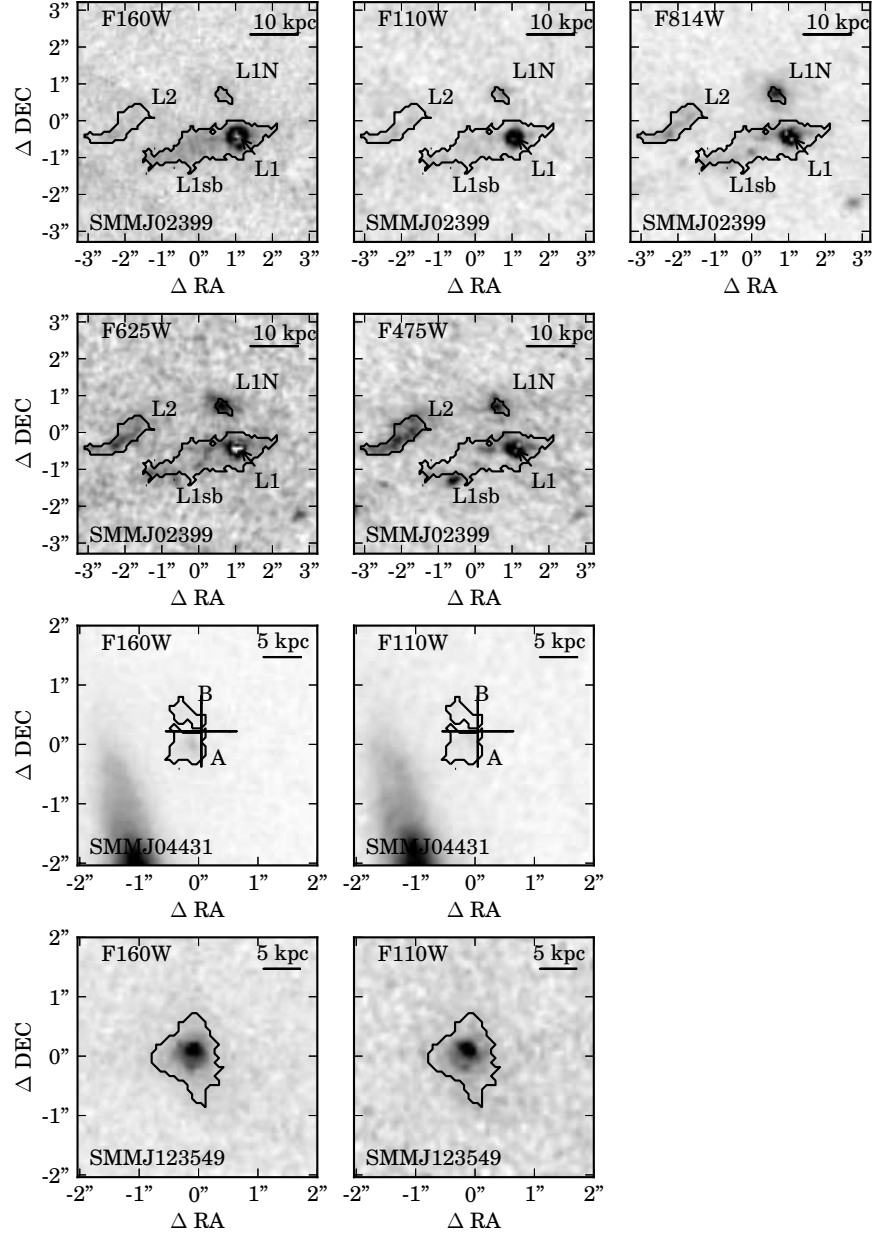


Fig. 1.— Near-infrared and optical *HST* images (when available) for our sample of ten SMGs, convolved to match the F160W PSF. Solid contours represent the boundaries of the segmentation regions used for the different components, as described in Section 4.3. Axis ticks indicate distance to the source center in arcseconds, and the scale bar indicates a reference distance in kpc at the source’s redshift, before correcting for lensing magnification. North is up and east is to the left. For SMM J02399–0136, the point-source model for the AGN located in L1 has been subtracted from all images. In plots for SMM J04431+0210, the cross indicates the centroid of the CO(3–2) emission measured by Tacconi et al. (2006) with the total combined position error bars. For SMM J14011+0252, we show the F850LP image before (fourth panel) and after (third panel) subtraction of the foreground source J1c to demonstrate the results of our GALFIT modelling (see Section 4.2.1). For F110W and F160W we present the final images with J1c removed.

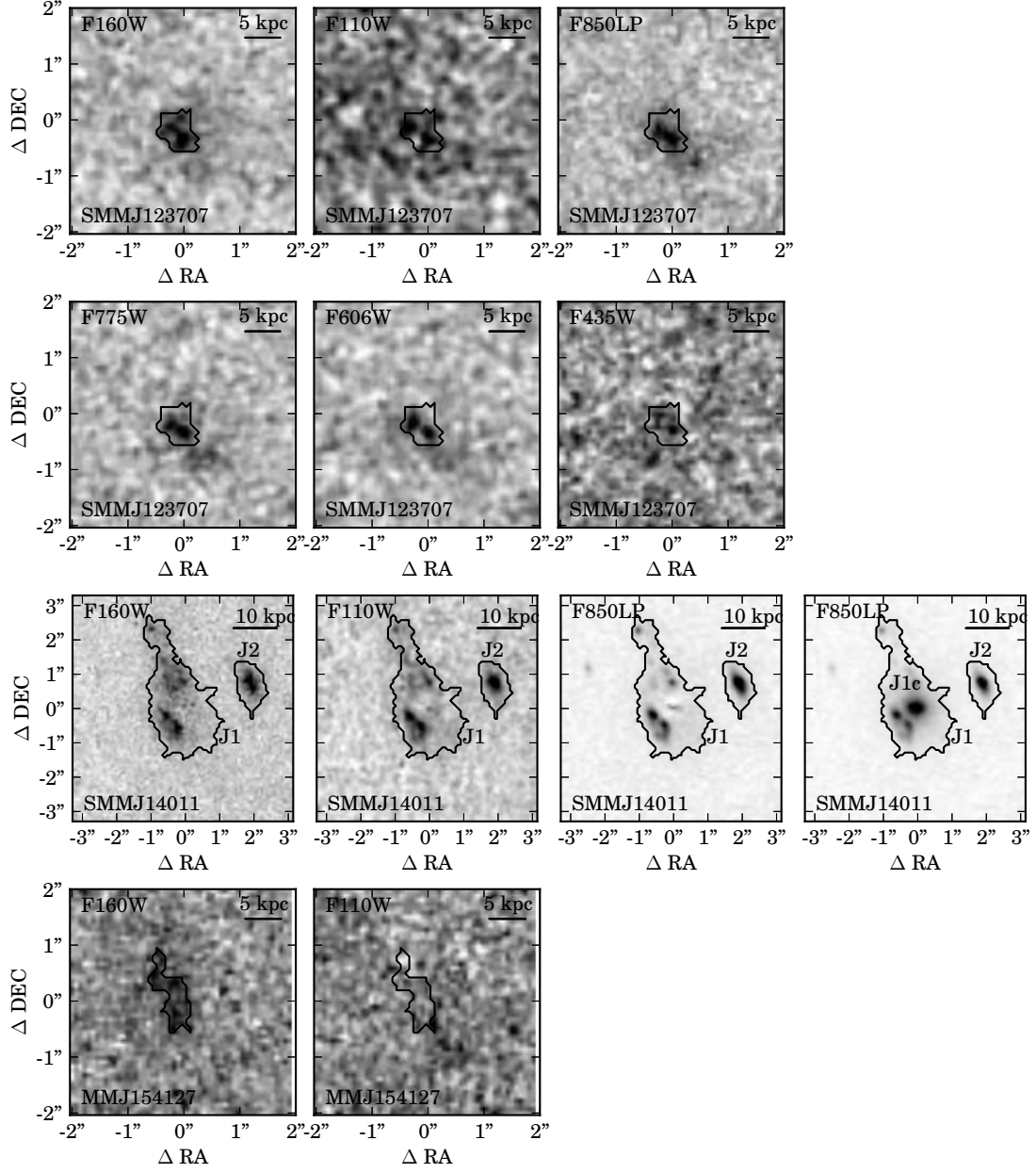


Fig. 1.— (continued)

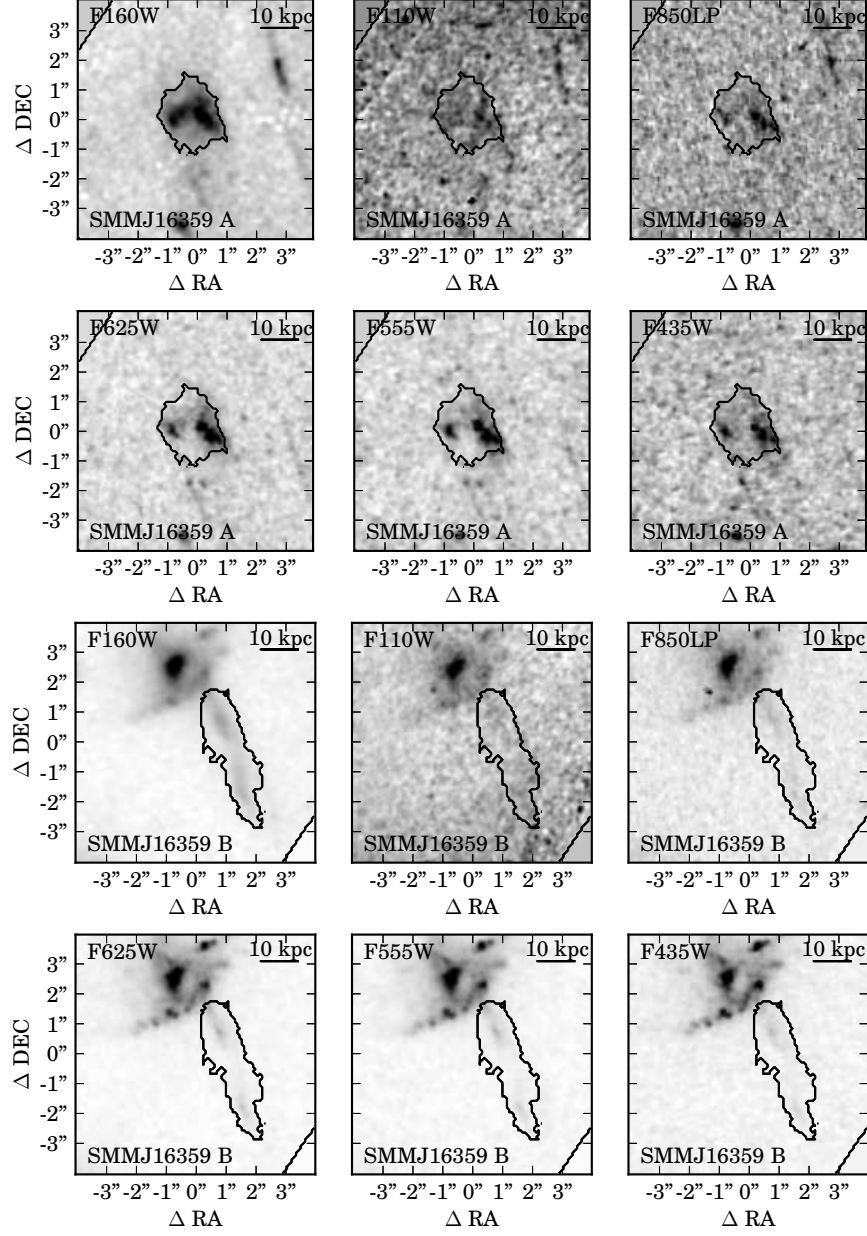


Fig. 1.— (continued)

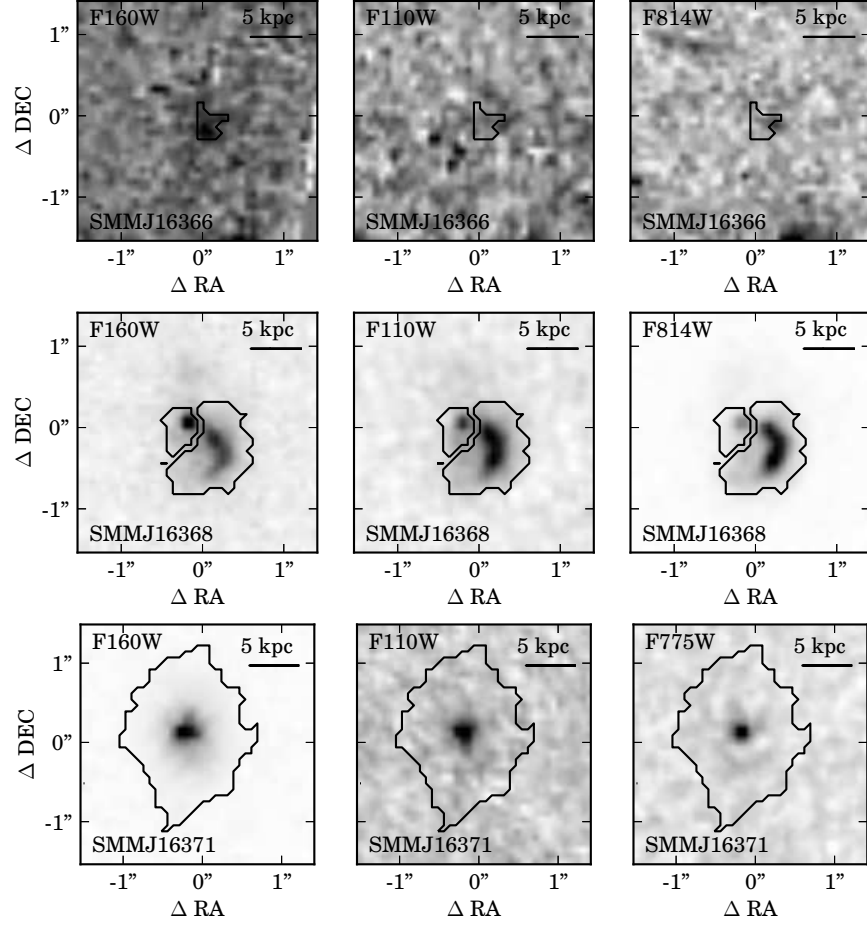


Fig. 1.— (continued)

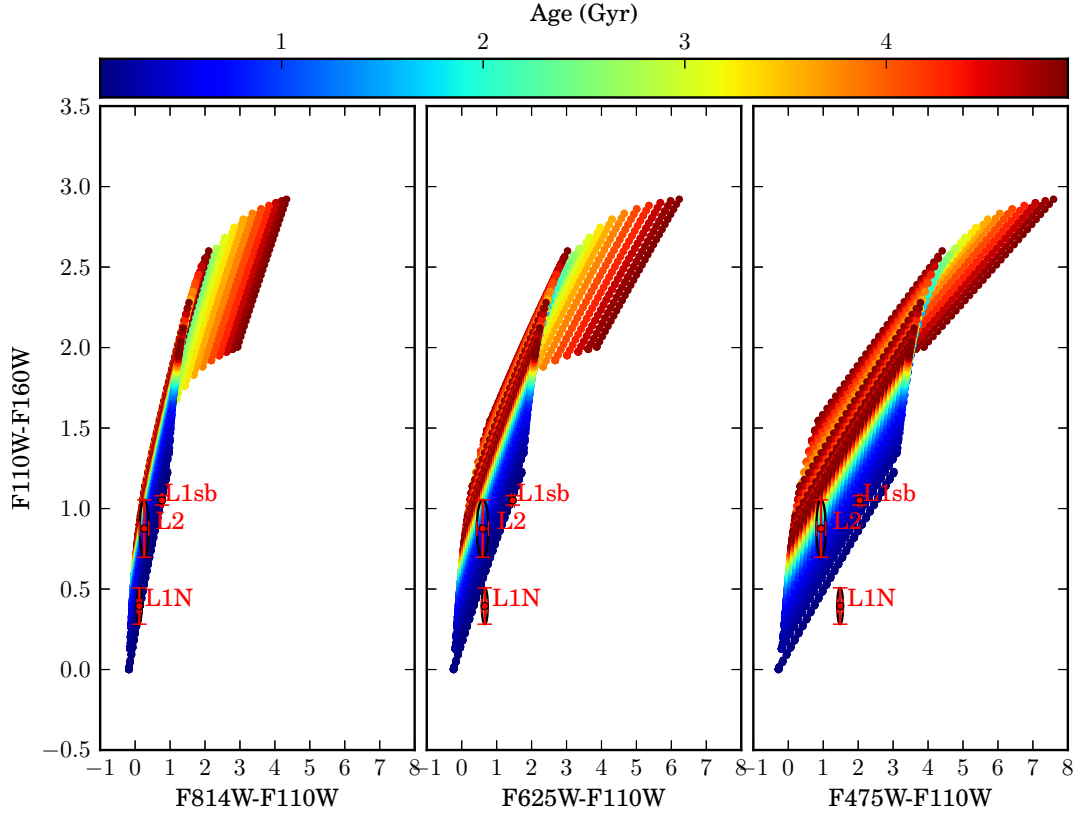


Fig. 2.— Color–color plots at the redshift of SMM J02399–0136, for stellar population models with exponential star formation timescales between 0 and 5 Gyr and visual extinctions between 0 and 5 mag. Color bar represents the age in Gyr; error bars represent the 1σ photometric errors, and ellipses indicate the locations of all stellar population models that are consistent within 1σ with the magnitudes measured for each component of SMM J02399–0136. A color version of this figure is available in the online journal.

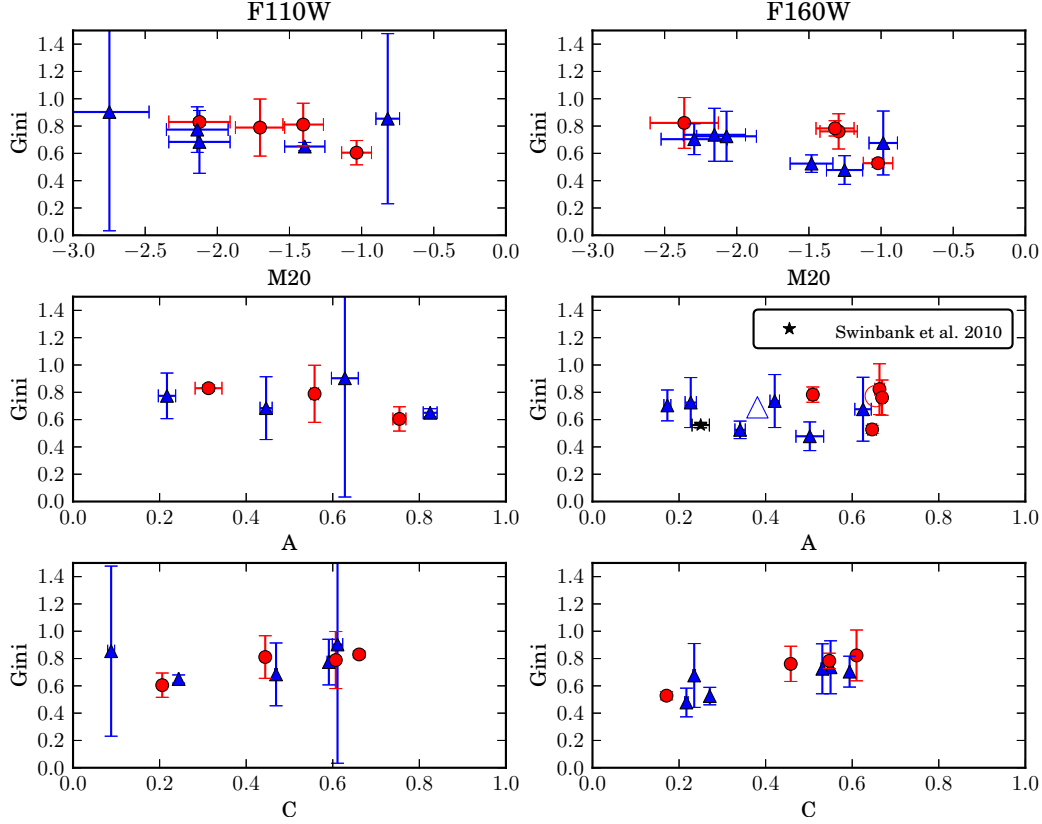


Fig. 3.— Morphological parameters measured in bands F160W and F110W for all targets, with their associated uncertainties. Dots correspond to targets classified as multi-component objects, and triangles represent single-component objects. In the center-right panel, we also plot the median value measured by Swinbank et al. (2010b) as a star, and the median values for multi-component and single-component objects as an open dot and triangle, respectively.

Table 1. Near-infrared Observations.

Target	R.A. (J2000)	decl. (J2000)	z	Instrument		Integration time (s)	
				F110W	F160W	F110W	F160W
SMM J02399–0136	02:39:52.00	−01:35:59.00	2.81	NIC2	NIC2	2560	2560
SMM J04431+0210	04:43:07.10	+02:10:25.00	2.51	NIC2	NIC2	2560	2560
SMM J123549.44+621536.8	12:35:49.40	+62:15:37.00	2.20	NIC2	NIC2	2688	2688
SMM J123707+621410	12:37:07.20	+62:14:08.00	2.49	NIC2	NIC2	2688	2688
SMM J14011+0252	14:01:04.90	+02:52:24.00	2.56	NIC2	NIC2	2560	2560
MM J154127+6616	15:41:27.80	+66:16:17.00	2.79	NIC2	NIC2	2688	2688
SMM J16359+6612	16:35:54.48	+66:12:30.50	2.52	NIC2	WFC3	2688	2612
SMM J16368+4057	16:36:50.40	+40:57:34.00	2.38	NIC2	NIC2 ^a	2560	2303
SMM J16366+4105	16:36:58.20	+41:05:24.00	2.45	NIC2	NIC2 ^a	2560	2303
SMM J16371+4053	16:37:06.50	+40:53:14.00	2.38	NIC2	WFC3	2560	2412

^aData retrieved from *HST* archive (PID:9856).

Table 2. Optical Observations

Target	Filter	Integration Time (s)	PID
SMM J02399–0136	F475W	6780	11507
	F625W	2040	11507
	F814W	3840	11507
SMM J123707+621410	F435W	79200	9583
	F606W	55280	9583
	F775W	87950	9583
	F850LP	254720	9583
SMM J14011+0252	F850LP	9110	10154
SMM J16359+6612	F435W	5640	9717
	F555W	5640	9717
	F625W	5640	9717
	F850LP	2680	9292
SMM J16368+4057	F814W	4760	9761
SMM J16366+4105	F814W	4284	9761
SMM J16371+4053	F775W	2064	9856

Table 3. Photometry Results.

Object	Filter	m_{AB}	Object	Filter	m_{AB}
SMM J02399–0136 L1N	F160W	25.02 ± 0.07	MM J154127+6616	F160W	23.79 ± 0.05
	F110W	25.46 ± 0.04		F110W	≥ 25.70
	F814W	25.56 ± 0.02	SMM J16359+6612 A	F160W	25.03 ± 0.02
	F625W	26.10 ± 0.04		F110W	26.01 ± 0.08
	F475W	26.92 ± 0.04		F850LP	26.10 ± 0.07
SMM J02399–0136 L2	F160W	24.45 ± 0.06		F625W	26.28 ± 0.02
	F110W	25.01 ± 0.04	SMM J16359+6612 B	F555W	26.51 ± 0.03
	F814W	25.25 ± 0.02		F435W	27.03 ± 0.04
	F625W	25.57 ± 0.03		F160W	25.08 ± 0.01
	F475W	25.64 ± 0.03		F110W	25.69 ± 0.05
SMM J02399–0136 L1sb	F160W	21.85 ± 0.01		F850LP	26.08 ± 0.04
	F110W	22.89 ± 0.02	SMM J16368+4057 B	F625W	26.37 ± 0.01
	F814W	23.63 ± 0.01		F555W	26.53 ± 0.02
	F625W	24.31 ± 0.03		F435W	27.04 ± 0.03
	F475W	24.89 ± 0.02		F160W	21.88 ± 0.01
SMM J04431+0210 A	F160W	24.72 ± 0.04	SMM J16368+4057 C	F110W	22.63 ± 0.01
	F110W	25.83 ± 0.07		F814W	22.64 ± 0.00
SMM J04431+0210 B	F160W	25.83 ± 0.07		F160W	22.92 ± 0.02
	F110W	26.94 ± 0.13	SMM J16366+4105	F110W	24.06 ± 0.02
SMM J123549.44+621536.8	F160W	21.92 ± 0.01		F814W	22.63 ± 0.01
	F110W	22.80 ± 0.02		F160W	24.41 ± 0.08
SMM J123707+621410	F160W	23.30 ± 0.03	SMM J16371+4053	F110W	≥ 25.58
	F110W	25.08 ± 0.07		F814W	≥ 27.17
	F850LP	25.57 ± 0.04		F160W	21.93 ± 0.01
	F775W	26.15 ± 0.05		F110W	23.66 ± 0.07
	F606W	26.85 ± 0.06		F775W	24.40 ± 0.06
SMM J14011+0252 J1	F435W	≥ 27.73			
	F160W	22.58 ± 0.08			
	F110W	23.41 ± 0.09			
	F850LP	23.56 ± 0.05			
SMM J14011+0252 J2	F160W	23.92 ± 0.10			
	F110W	24.66 ± 0.11			
	F850LP	24.49 ± 0.06			

Note. — We report the magnitudes or limits measured inside the segmentation regions defined as described in Section 4.3. All magnitudes are corrected for gravitational magnification using the amplification factors quoted in the text.

Table 4. Morphological Parameters Calculated from F160W and F110W Images of Our Targets.

Object	μ	$r_h(\text{kpc})$	F160W				$r_h(\text{kpc})$	F110W				S/M
			A	C	G	M_{20}		A	C	G	M_{20}	
SMM J02399–0136	2.4	3.89	0.66	0.61	0.82	-2.36	1.65	0.31	0.66	0.83	-2.12	M
SMM J04431+0210	4.4	3.67	0.65	0.17	0.53	-1.02	3.63	0.75	0.21	0.60	-1.03	M
SMM J123549+621536	...	3.21	0.42	0.55	0.74	-2.15	3.66	0.45	0.47	0.68	-2.12	S
SMM J123707+621410	...	2.78	0.34	0.27	0.53	-1.48	3.19	0.82	0.24	0.65	-1.39	S
SMM J14011+0252 J1	4.0	8.36	0.67	0.46	0.76	-1.29	7.95	1.04	0.44	0.81	-1.41	M
SMM J14011+0252 J2	3.5	2.82	0.23	0.53	0.72	-2.07	1.89	0.22	0.59	0.77	-2.14	M
MM J154127+6616	...	3.55	0.62	0.23	0.68	-0.98	S
SMM J16368+4057	...	2.76	0.51	0.55	0.78	-1.32	3.07	0.56	0.61	0.79	-1.70	M
SMM J16366+4105	...	1.81	0.38	0.22	0.48	-1.25	S
SMM J16371+4053	...	3.36	0.17	0.59	0.70	-2.29	2.30	0.63	0.61	0.90	-2.75	S

Note. — Objects MM J154127+6616 and SMM J16366+4105 were not detected in F110W, so their morphologies were only studied in F160W. In the second column we indicate the magnification factors μ assumed for lensed objects; r_h corresponds to the circularized radius, calculated as $r_h = \sqrt{a_h b_h}$, where a_h and b_h are the major and minor half light radii measured from the images. The last column indicates whether the object was classified as a single (S) or multiple (M) component system. SMMJ16359+6612 is excluded from the morphological analysis due to its strong distortion by the gravitational potential.

Table 5. Stellar Masses, Derived Using a Chabrier (2003) IMF.

Object	$\log_{10}(M_*/M_\odot)$	Mass ratio	S/M
SMM J02399–0136 L1sb	11.8 ± 0.1		M
SMM J02399–0136 L2	10.1 ± 0.1	50.1	
SMM J02399–0136 L1N	9.7 ± 0.1	125.8	
SMM J04431+0210 A	10.0 ± 0.3		M
SMM J04431+0210 B	9.6 ± 0.4	2.5	
SMM J123549+621536	10.8 ± 0.3	...	S
SMM J123707+621410	11.3 ± 0.1	...	S
SMM J14011+0252 J1	10.5 ± 0.2		M
SMM J14011+0252 J2	9.8 ± 0.3	5.0	
MM J154127+6616	S
SMM J16359+6612 A	9.6 ± 0.2	...	S
SMM J16368+4057 B	10.6 ± 0.2		M
SMM J16368+4057 C	10.7 ± 0.2	1.3	
SMM J16366+4105	11.8 ± 0.2	...	S
SMM J16371+4053	11.7 ± 0.1	...	S

Note. — In the second column we report the stellar masses of the individual components identified in multiple systems, and in the third column we give the mass ratio. The third column is repeated from Table 4, and indicates whether an object was classified as a single (S) or multiple (M) system.